



*AGU Advances*

Second Version of

**Subantarctic Mode Water Biogeochemical Formation Properties and Interannual Variability**

Seth M. Bushinsky and Ivana Cerovečki

<sup>1</sup> Department of Oceanography, School of Ocean and Earth Science and Technology, University of Hawai'i at Mānoa, Honolulu, HI

<sup>2</sup> Scripps Institution of Oceanography, University of California San Diego, La Jolla, CA

1           **Subantarctic Mode Water Biogeochemical Formation Properties and Interannual**  
2                                   **Variability**

3

4   Seth M. Bushinsky<sup>1</sup> and Ivana Cerovečki<sup>2</sup>

5

6   <sup>1</sup>Department of Oceanography, School of Ocean and Earth Science and Technology, University  
7   of Hawai‘i at Mānoa, Honolulu, HI

8   <sup>2</sup>Scripps Institution of Oceanography, University of California San Diego, La Jolla, CA

9

10   Corresponding author: Seth Bushinsky (seth.bushinsky@hawaii.edu)

11

12   **Key Points:**

- 13           • Subantarctic Mode Water (SAMW) biogeochemical formation properties are a function  
14           of the density of newly formed water  
15           • Newly formed SAMW is undersaturated in oxygen due to opposing effects from cooling  
16           (solubility) and entrainment, and air-sea injection  
17           • SAMW is near or above atmospheric  $p\text{CO}_2$  during formation and therefore not a strong  
18           direct sink of contemporary carbon dioxide  
19

20

21

**Abstract**

Subantarctic Mode Water (SAMW) is a key water mass for the transport of nutrients, oxygen, and anthropogenic carbon into the ocean interior. However, a lack of biogeochemical observations of SAMW properties during wintertime formation precluded their detailed characterization. Here we characterize for the first time SAMW properties across their entire wintertime formation regions based primarily on biogeochemical profiling floats. Observations show that the SAMW properties differ between the two main formation regions in the Pacific and Indian sectors of the Southern Ocean. SAMW formed in the Pacific is colder, fresher, and higher in oxygen, nitrate, and dissolved inorganic carbon than its Indian Ocean counterpart. The relationship between potential density and biogeochemical water properties is nearly identical between the two formation regions; property differences thus predominantly reflect the difference in mean densities of SAMW formed in each region. SAMW is undersaturated in oxygen during formation, which will impact calculations of derived quantities that assume preformed oxygen saturation. SAMW is at or above atmospheric  $p\text{CO}_2$  during wintertime and therefore not a direct sink of contemporary carbon dioxide during the formation period. Results from the Biogeochemical Southern Ocean State Estimate suggest anti-correlated interannual variability in dissolved inorganic carbon, nitrate, and oxygen in the central and southeastern Pacific formation regions similar to previously established patterns in mixed layer physical properties. This indicates that the mean properties of SAMW will vary depending on which sub-region has a stronger formation rate, which is in turn linked to the Southern Annual Mode and the El-Niño Southern Oscillation.

43

**Plain Language Summary**

In the Southern Ocean, north of the Antarctic Circumpolar Current, wintertime surface ocean heat loss cools the water, increasing its density and forming thick layers of well mixed water that enter the ocean. This water, called Subantarctic Mode Water (SAMW), represents an important pathway for anthropogenic carbon, nutrients and oxygen into the ocean interior. In this study we used new wintertime observations from profiling robots equipped with sensors that measure oxygen, nitrate, and pH in the top 2000 m to determine important initial properties of SAMW for the first time. We find that the SAMW properties differ between the Pacific and Indian formation regions and are related to the densities of SAMW formed in each basin. These properties indicate

53 that it is unlikely for SAMW to take up present-day carbon dioxide from the atmosphere during  
54 formation, though it may still absorb anthropogenic carbon. We investigated how these  
55 properties varied year-to-year using an ocean model linked to observations, finding connections  
56 between changes in the biogeochemical properties and physical processes as well as large-scale  
57 climate variability. These results will provide valuable constraints on interpretation of subsurface  
58 ocean measurements and model studies investigating the role of these waters in the global carbon  
59 cycle.

60

61

62

## 63 1. Introduction

64 The Southern Ocean (south of 35°S) is responsible for approximately 50% of the  
65 contemporary carbon absorbed by the ocean each year (Landschützer et al. 2015, 2016; Gruber et  
66 al. 2019b). This Southern Ocean contemporary carbon uptake is largely driven by a strong  
67 anthropogenic carbon flux (Mikaloff Fletcher et al. 2006; DeVries 2014) overlaid on a balanced  
68 natural carbon cycle (Gruber et al. 2019b). North of the Antarctic Circumpolar Current (ACC),  
69 the uptake of natural carbon is driven by Thermocline Waters (TW) from the subtropics that cool  
70 as they are advected south and are the site of biological production, both of which lower the  
71 partial pressure of CO<sub>2</sub> ( $p\text{CO}_2$ ) in the ocean, drawing down carbon from the atmosphere  
72 (Mikaloff Fletcher et al. 2007; Gruber et al. 2009b, 2019b). This uptake is balanced by the  
73 upwelling of Circumpolar Deep Water (CDW) enriched in old carbon from degraded biological  
74 material that is released to the atmosphere as CDW waters reach the surface south of the ACC. A  
75 fraction of the upwelled CDW is advected southward, where it cools and subducts as Antarctic  
76 Bottom Water, while another fraction is advected northward, mixing with TWs advected  
77 southward, forming mode and intermediate waters (Iudicone et al. 2011; Morrison et al. 2015).  
78 Newly formed Subantarctic Mode Water (SAMW) contains a mix of CDW, Antarctic  
79 Intermediate Water (AAIW), older SAMW that is re-entrained as intense surface heat loss during  
80 the winter drives deep winter mixed layers and subduction, and TW (McCartney 1977; Hanawa  
81 and Talley 2001). After subduction, these well-mixed, near-surface layers are advected away  
82 from their formation regions into the ocean interior (McCartney 1977, 1982). SAMW primarily  
83 forms in the Indian and Pacific sectors of the Southern Ocean, where wintertime mixed layers are  
84 deepest (Figure 1).

85 After subduction, SAMW is advected by the ACC and can either be re-entrained and  
86 modified during subsequent winter mixed layer (ML) deepening or exported into the ocean  
87 interior where it is advected by the subtropical gyre circulation (Hanawa and Talley 2001; Koch-  
88 Larrouy et al. 2010; Hartin et al. 2011; Cerovečki et al. 2019; Morrison et al. 2022). SAMW  
89 redistributes heat and freshwater from the Southern Ocean to the tropics (Wong et al. 1999) and  
90 the export of nutrients from the Southern Ocean through mode and intermediate waters fuels  
91 between 44 and 75% of global ocean productivity (Sarmiento et al. 2004; Primeau et al. 2013).  
92 SAMW is also one of the major water masses that transports anthropogenic and natural carbon  
93 into the ocean interior from the Southern Ocean, based on interior measurements of dissolved

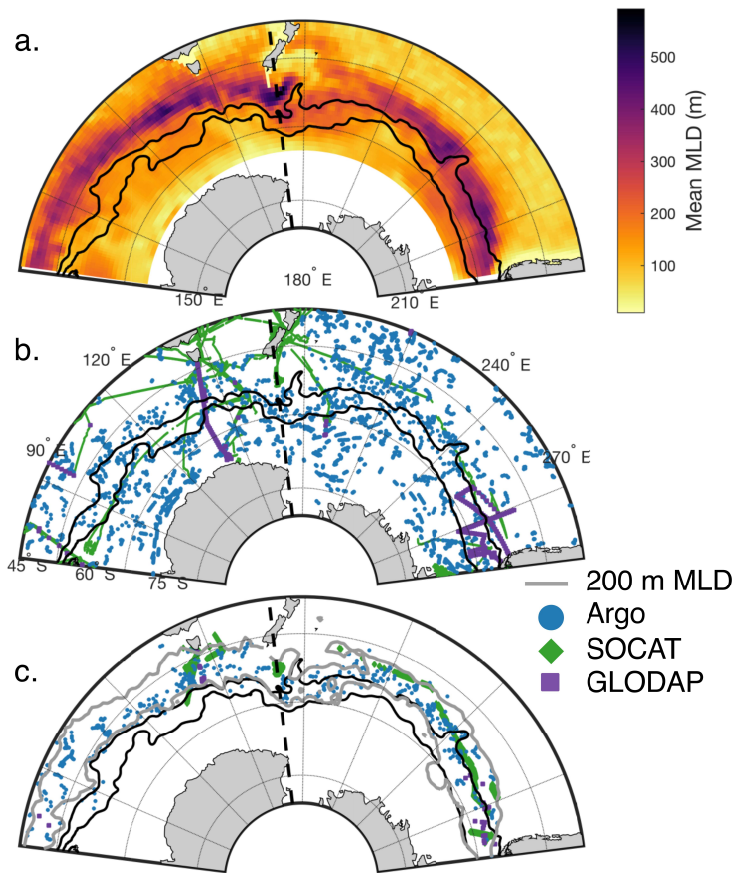


**Figure 1. Wintertime mixed layer depths (MLD) and distribution of wintertime observations in the Indian and Pacific sectors of the Southern Ocean.** (a) Mean winter (Aug-Sept) mixed layer depth calculated from gridded Argo product 2005-2020 (RG-Argo). (b) Map of wintertime water column biogeochemical properties (Argo floats, blue dots; GLODAP dataset since 1990, purple squares) and  $p\text{CO}_2$  surface measurements (SOCAT dataset since 1990, green squares). (c) Same as (b), but only showing data within the SAMW density ranges in the Pacific ( $26.8 \leq \sigma_\theta < 27.05 \text{ kg m}^{-3}$ ) and Indian ( $26.6 \leq \sigma_\theta < 26.9 \text{ kg m}^{-3}$ ) basins within the wintertime mixed layer depths  $\geq 200 \text{ m}$ . The gray contour represents the mean wintertime 200 m MLD from RG-Argo indicating mode water formation regions. Black lines in all plots are the Polar Front (southern line) and the Subantarctic Front (Orsi et al. 1995). Black dashed line indicates separation

94 inorganic carbon (DIC) and modeling inversion studies (Mikaloff Fletcher et al. 2006, 2007;  
 95 Gruber et al. 2009b, 2019b). Southern Ocean mode and intermediate waters help ventilate the  
 96 ocean interior with oxygen (Russell and Dickson 2003; Carter et al. 2014) and their distinctive  
 97 high oxygen signature is evident as they spread into the subtropical gyre (McCartney 1977;  
 98 Hanawa and Talley 2001). Modeling results indicate that SAMW has accumulated  $\sim 20\%$  of the  
 99 total ocean anthropogenic carbon inventory and gains  $\sim 28\%$  of the annual anthropogenic carbon  
 100 increase, with 60-86% of the increase coming from air-sea fluxes and the rest accumulated  
 101 through interior diapycnal processes (Groeskamp et al. 2016; Iudicone et al. 2016). However, the  
 102 mechanistic understanding of air-sea  $\text{CO}_2$  fluxes that we gain from model simulations are  
 103 dependent on accurate model representation of preformed mode water biogeochemical properties  
 104 and resulting air-sea fluxes for which validation data has been previously unavailable.

105 SAMW is not homogeneous in space, but instead consists of pools of water with distinct  
 106 properties that form in different locations. SAMW is then exported to the subtropics from these  
 107 well-defined “hotspots” of formation following distinct pathways influenced by topography  
 108 (Koch-Larrouy et al. 2010; Herraiz-Borreguero and Rintoul 2011; Li et al. 2021). While many

109 physical processes play an important role in SAMW formation, air-sea buoyancy fluxes and  
110 Ekman transport of cold water are generally considered to be dominant (Speer et al. 2000;  
111 Sloyan and Rintoul 2001; Rintoul and England 2002). SAMW is strongly coupled to the  
112 atmosphere and the interannual variability of wintertime atmospheric forcing governs the  
113 interannual variability and regional distribution of SAMW formation in the Pacific and Indian  
114 sectors of the Southern Ocean, as revealed by the Argo observations. In the Southern  
115 Hemisphere the extratropical atmospheric circulation has the quasi-stationary zonal wave  
116 number 3 (ZW3) pattern present in both the mean atmospheric circulation and its variability on  
117 daily, seasonal, and interannual timescales (Raphael 2004). As SAMW is strongly coupled to the  
118 atmosphere, the ZW3 can also be imprinted onto the zonal distribution of deep wintertime mixed  
119 layers associated with SAMW formation (Meijers et al. 2019; Tamsitt et al. 2020; Cerovečki and  
120 Meijers 2021). The ZW3 pattern is a prominent feature in the winter quasi-stationary mean sea  
121 level pressure (MSLP) anomalies (Cerovečki and Meijers 2021). The meridional wind anomalies  
122 introduced by these MSLP anomalies are of the opposite sign on the two flanks of each center of  
123 the MSLP anomaly, resulting in anomalously cold conditions and deep mixed layers on the flank  
124 with enhanced southerly winds, and anomalously warm conditions and shallow mixed layers on  
125 the flank with enhanced northerly winds. Thus in years with strong wintertime MSLP anomalies  
126 in the SAMW formation latitude range, deep wintertime mixed layer depth (MLD) anomalies  
127 have a dipole pattern in each of the three ocean sectors, and these MLD anomalies in the three  
128 ocean sectors tend to be in phase, which results in a more circumpolar response to the  
129 atmospheric forcing (Tamsitt et al. 2020; Cerovečki and Meijers 2021). Argo observations have  
130 also revealed that the variability of mode water volume and properties in SAMW pools is  
131 governed not only by local atmospheric forcing, but also by advective processes that transport  
132 property anomalies eastward, with a  $\sim 1$  year lag between the central and southeastern Pacific  
133 (Meijers et al. 2019; Cerovečki et al. 2019).

134 SAMW variability is strongly linked to the dominant modes of variability in the Southern  
135 Hemisphere. The Southern Annual Mode (SAM) leads to large-scale wintertime MLD anomalies  
136 (Sallée et al. 2010), strongly influencing the volume of subducted mode water. This volume has  
137 increased over the Argo period (Gao et al. 2018; Portela et al. 2020) as mixed layers have  
138 deepened in response to a strengthening SAM (Qu et al. 2020). In the Pacific, SAMW formation

139 is also influenced by El Niño–Southern Oscillation (ENSO), and the relative phases of the ENSO  
140 and SAM governs the interannual variability of SAMW thickness (Meijers et al. 2019).

141 In contrast to physical properties, changes in large-scale Southern Ocean biogeochemical  
142 properties in response to climate variability, including those of SAMW, have primarily been  
143 described using the results of model simulations. Modeling studies have linked decreased  
144 contemporary Southern Ocean CO<sub>2</sub> fluxes and elevated surface DIC concentrations to positive  
145 SAM phase through increased Ekman-driven upwelling of old waters enriched in DIC (Lenton  
146 and Matear 2007; Lovenduski et al. 2007). Verdy et al. (2007) explored climate drivers of  
147 oxygen and CO<sub>2</sub> fluxes in the Southern Ocean using a global numerical ocean model. The Pacific  
148 dipole described in Meijers et al. (2019) and Cerovečki and Meijers (2021) is evident in the first  
149 EOF of both oxygen and CO<sub>2</sub> flux variability in Verdy et al. (2007), which the authors also  
150 associate with SAM. The upwelling of low oxygen water drives oceanic uptake of oxygen, so the  
151 response has the opposite sign from CO<sub>2</sub>. They find that ENSO is a secondary driver of oxygen  
152 and CO<sub>2</sub> flux variability in the Pacific, though with a similar magnitude of induced oxygen and  
153 CO<sub>2</sub> fluxes and a dipole structure still evident.

154 Wintertime measurements of biogeochemical tracers in the Southern Ocean are limited,  
155 with most of the shipboard measurements that have historically underpinned our understanding  
156 of ocean properties concentrated in a few locations (Figure 1). Therefore, despite their  
157 importance for determining the distribution of carbon, nutrients, and oxygen in the ocean  
158 interior, the biogeochemical properties of SAMW at the time of formation are poorly  
159 characterized. Knowing water mass formation properties is key to interpreting downstream  
160 biogeochemical measurements and ground-truthing the model-based interpretations of the role of  
161 SAMW in nutrient export and anthropogenic carbon uptake. The impact of nutrients exported by  
162 SAMW to the global ocean on air-sea carbon dioxide fluxes is determined by whether, once  
163 upwelled to the surface, those nutrients are preformed or sourced from biological material that  
164 degraded sometime between initial subduction and eventual re-emergence in the upper ocean.  
165 Nutrient regeneration from respiration is accompanied by the release of DIC and consumption of  
166 oxygen, such that biological production fueled by regenerated nutrients will either be offset by  
167 regenerated CO<sub>2</sub> outgassing or will re-fix the regenerated DIC back to organic carbon. Preformed  
168 nutrients are not coupled to regenerated DIC and can fuel net carbon uptake from the atmosphere  
169 when next upwelled to the surface. Preformed nutrients are often estimated using oxygen



170 measurements, an oxygen consumption to nutrient release respiration ratio, and assumed oxygen  
171 saturation during formation. It is therefore important to characterize oxygen and preformed  
172 nutrients present in different water masses and to understand if and how they vary in time.

173 Only one study has analyzed formation properties of SAMW from shipboard  
174 measurements made on individual cruises that crossed a SAMW formation region in the  
175 southeast Pacific (Carter et al. 2014). Recent deployments of profiling floats equipped with  
176 biogeochemical sensors throughout the Southern Ocean by the Southern Ocean Carbon and  
177 Climate Observations and Modeling project (SOCCOM; Johnson et al. 2017) offer a new  
178 opportunity to characterize these waters and better understand the role that SAMW plays in the  
179 global carbon cycle and production.

180 While mapped interpolation products are available for some biogeochemical variables  
181 (Garcia et al. 2010; Landschützer et al. 2013; Rödenbeck et al. 2013; Lauvset et al. 2016) these  
182 products are biased toward summertime measurements. For example, inclusion of float-derived  
183  $p\text{CO}_2$  with ship-board observations in standard mapping methods has reduced estimates of the  
184 annual Southern Ocean contemporary carbon uptake from an annual uptake of  $\sim 1.1 \text{ Pg C yr}^{-1}$  to  
185  $0.75 \pm 0.22 \text{ Pg C yr}^{-1}$  (Bushinsky et al. 2019), primarily due to new wintertime observations.  
186 Furthermore, the wintertime formation of SAMW has strong temporal and spatial variability,  
187 leading to possible biases if properties or variability are extrapolated from too-sparse  
188 measurements (Fay et al. 2014). These float-derived year-round, vertically-resolved  
189 biogeochemical measurements for the first time enable characterization of these important water  
190 masses during formation and will provide the link between surface processes and interior ocean  
191 properties and changes. In this study we use wintertime observations from profiling floats and  
192 available shipboard measurements to characterize SAMW properties at the time of formation.  
193 Using results of an ocean state estimate we determine how these properties vary interannually  
194 and regionally prior to export into the global ocean.

195

## 196 **2. Methods**

### 197 **2.1 SAMW identification**

198 SAMW was identified from gridded Argo T&S (hereafter RG-Argo; Roemmich and  
199 Gilson 2009) using a potential vorticity (PV) threshold of  $PV < 40 \times 10^{-12} \text{ (m s)}^{-1}$ , with PV  
200 defined as  $PV = f/\rho \partial\sigma_\theta/\partial z$ , where  $f$  is the Coriolis parameter,  $\rho$  is the density of seawater,

201 and  $\sigma_\theta$  is the potential density (taken here to be defined relative to the surface), averaged over  
202 the years 2005-2020. This PV threshold was used to identify the density range of core SAMW in  
203 the Pacific (170°E to 70°W, 64°S to 45°S) and Indian (68°E to 170°E, 55°S to 30°S) ocean  
204 sectors, identified as density bins (0.05 kg m<sup>-3</sup>-wide spacing) containing at least 5% of total  
205 SAMW volume in an annual average. We then used these density ranges throughout the rest of  
206 the study to identify wintertime SAMW in each basin.

207

## 208 **2.2 Biogeochemical observations**

209 Biogeochemical properties of the deep wintertime mixed layers that form SAMW were  
210 determined from biogeochemical Argo float observations obtained from two sources. The  
211 primary dataset is observations from over 200 floats equipped with oxygen, nitrate, pH, and bio-  
212 optical sensors deployed by SOCCOM since 2014 (May 2021 snapshot; Johnson et al., 2017).  
213 The SOCCOM data are supplemented by the University of Washington Argo Oxygen dataset  
214 (UW Argo O<sub>2</sub>; v1.1; Drucker and Riser, 2016) that contains post-adjusted Argo oxygen data  
215 from 2003 to 2014. Where float data was present in both datasets the SOCCOM data were  
216 preferentially used. The final dataset contains 311 floats, of which 53 contain profiles that fell  
217 within the criteria used to define SAMW formation periods. A profile was determined to have  
218 sampled the SAMW formation period if it fell within the density range for a given basin, was  
219 from August or September, and had a calculated MLD of at least 200 m.

220 Oxygen and nitrate in the SOCCOM dataset are measured by sensors mounted on the  
221 floats with stated uncertainties of 1-2  $\mu\text{mol kg}^{-1}$  for oxygen and  $<1 \mu\text{mol kg}^{-1}$  for nitrate (Johnson  
222 et al. 2017). Oxygen uncertainties from the UW Argo O<sub>2</sub> dataset are  $\sim 1\%$ , or  $\sim 3 \mu\text{mol kg}^{-1}$  at the  
223 concentrations observed in this study. The partial pressure of carbon dioxide ( $p\text{CO}_2$ ) and  
224 dissolved inorganic carbon (DIC) are estimated in the SOCCOM data processed stream from  
225 measured pH and an alkalinity multiple linear regression (Williams et al. 2017; Carter et al.  
226 2018) with a theoretical uncertainty of  $\sim 11 \mu\text{atm}$  for  $p\text{CO}_2$ , and  $\sim 6 \mu\text{mol kg}^{-1}$  for DIC (Williams  
227 et al. 2017, 2018; Johnson et al. 2017). While float observations underwent prior QC, a  
228 secondary QC was performed by checking time series of temperature, salinity, oxygen, nitrate,  
229 pH, and derived  $p\text{CO}_2$  in the upper 20 m for each float. Large spikes in individual properties with  
230 no accompanying changes in related properties were removed from analysis (Supplemental  
231 Table S1, 116 profiles removed out of 36,247 profiles total).

232

### 233 **2.3 Shipboard observations and derived quantities**

234 Shipboard bottle measurements from the Global Ocean Data Analysis Project v2.2020  
235 (GLODAP; Key et al., 2015; Olsen et al., 2016) and underway  $p\text{CO}_2$  data from the Surface  
236 Ocean  $\text{CO}_2$  Atlas v2021 (SOCAT; Bakker et al., 2016) are used to supplement float  
237 observations.  $p\text{CO}_2$  was calculated from GLODAP DIC and alkalinity using CO2SYS (van  
238 Heuven et al. 2011) and the same carbonate system constants as used by the SOCCOM project  
239 (Williams et al. 2017). MLDs are calculated for each float and ship profile using a  $0.03 \text{ kg m}^{-3} \sigma_\theta$   
240 change from a 10 m reference (de Boyer Montégut et al. 2004). SOCAT  $p\text{CO}_2$  observations are  
241 underway measurements that are not associated with a vertical profile from which MLD could be  
242 calculated. Instead, SOCAT observations were matched to the closest  $1^\circ \times 1^\circ$  ML from  
243 objectively interpolated RG-Argo (Roemmich and Gilson 2009) MLDs .

244  $\Delta p\text{CO}_2$  (surface  $p\text{CO}_2$  minus atmospheric  $p\text{CO}_2$ ) values were calculated using the  
245 atmospheric  $\text{CO}_2$  mole fraction ( $x\text{CO}_2$ , NOAA Greenhouse Gas Marine Boundary Layer  
246 Reference; Dlugokencky et al. 2019) matched to the nearest latitude (see supplemental text S2).  
247 A correction for sea level pressure was applied using a mean annual cycle for each location  
248 calculated from a 10-year time series of National Centers for Environmental Prediction (NCEP;  
249 Kalnay et al., 1996) reanalysis sea level pressure and water vapor pressure calculated from SST  
250 and SSS (Zeebe and Wolf-Gladrow 2001). Oxygen saturation concentrations are calculated from  
251 observed temperature and salinity and García and Gordon (1992) solubility coefficients.

252

### 253 **2.4 Biogeochemical Southern Ocean State Estimate (BSOSE)**

254 The biogeochemical Southern Ocean State Estimate (BSOSE; Verdy and Mazloff 2017)  
255 is a coupled biogeochemical-sea-ice-ocean state estimate that assimilates physical and  
256 biogeochemical observations, including from biogeochemical profiling floats, creating a  
257 coherent picture of Southern Ocean processes that conserves mass and has closed budgets for  
258 biogeochemical properties. BSOSE is forced by optimized atmospheric reanalysis fields from  
259 ERA-Interim (Dee et al. 2011). We used iteration 135, covering 2013-2019 at  $1/6^\circ$  resolution, for  
260 analysis of interannual variability. Here we only analyze the spatial and temporal variability of  
261 SAMW in BSOSE output from the Pacific sector, where the spatial distribution of deep  
262 wintertime MLDs and SAMW formation regions in BSOSE iteration 135 agreed well with those

263 from RG-Argo. The Pacific region was additionally of interest because it reflected the impact of  
264 the strong 2015/2016 El Niño.

265

### 266 **3. Results and discussion**

#### 267 **3.1 SAMW formation properties**

268 The potential density bounds established for regional SAMWs were  $26.8 \leq \sigma_\theta < 27.05$  kg  
269  $\text{m}^{-3}$  in the Pacific sector and  $26.6 \leq \sigma_\theta < 26.9$  kg  $\text{m}^{-3}$  in the Indian sector. These density ranges  
270 agree well with those from the literature (e.g. Cerovečki and Meijers, 2021). We identified  
271 SAMW properties from float observations in the Pacific and Indian sectors during the time of  
272 formation using these density bounds and calculating mean mixed layer properties from August  
273 to September at the locations where the float profile mixed layer depth was at least 200 m. The  
274 depth criterion was used to isolate the deep wintertime mixed layers associated with SAMW  
275 formation from other shallower winter mixed layers, such as in areas of reventilation or  
276 seasonally formed water that does not connect to the ocean interior (Koch-Larrouy et al. 2010).  
277 The threshold value was determined by examining the individual float observations.

278 Pressure vs. time plots of individual floats capture the seasonal cycle of deep mixing in  
279 the winter, where the lighter density bound of SAMW outcrops at the surface and newly formed  
280 waters bring surface properties into the SAMW layer (Figure 2). As the mixed layer shoals in  
281 austral spring, these waters mix in the ocean interior with older SAMW. After leaving Pacific or  
282 Indian SAMW formation regions, floats often captured reventilation in other areas, such as float  
283 5904695 that captured moderate wintertime ML deepening in the western Pacific in 2017 (Figure  
284 2). The float was advected eastward by the ACC and captured the process of strong wintertime  
285 ML deepening in the Pacific in winters of 2018 and 2019. The subsequent year the float was  
286 advected through the Drake Passage into the Atlantic, where SAMW was reventilated, further  
287 modifying the properties of SAMW that were set prior to restratification and isolation from the  
288 atmosphere. The current study focuses only on the period of deep winter mixed layers and initial  
289 formation properties, leaving reventilation and other post-formation modification processes to  
290 later work.

291 Properties in the deep ( $> 200$  m) winter mixed layers were first averaged in density bins  
292 within the geographical bounds of each ocean sector and then weighted by volume to calculate  
293 mean and standard deviation (Table 1). SAMW formed in the Pacific Ocean is colder and

294 fresher, with higher oxygen, nitrate, DIC, and  $p\text{CO}_2$  than SAMW that forms in the Indian Ocean  
295 (Table 1,

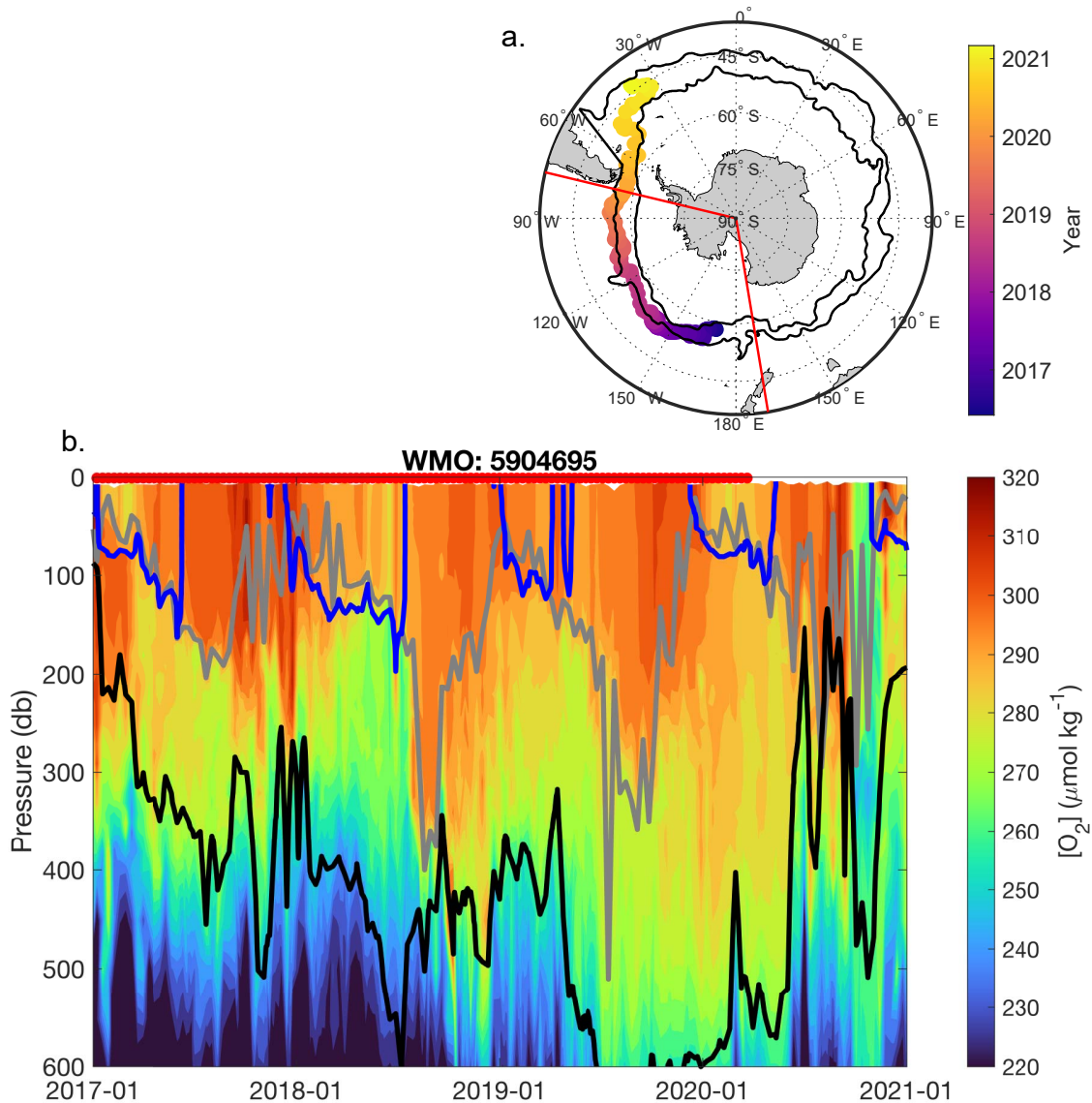


**Figure 2. Trajectory and oxygen measurements from float 5904695.** (a) Float 5904695 was deployed in the western Pacific in May 2016 and followed the Subantarctic Front (northern black line) as it was advected by the ACC into the Atlantic basin in 2020. Southern black line is the Polar Front. (b) Float oxygen measurements from the upper 600 m from 2017 to 2021. SAMW density bounds identified for the Pacific are shown for the lighter (blue,  $26.8 \text{ kg m}^{-3}$ ) and denser (black,  $27.05 \text{ kg m}^{-3}$ ) boundaries. MLD (gray) increases in the wintertime and the lighter SAMW boundary outcrops. MLs deeper than 200m were identified as waters likely to enter the ocean interior and therefore represent SAMW formation waters. This float captured both initial formation (for example in 2018 and 2019) as well as what appears to be subsequent reventilation in later years as the float passed into the Atlantic Ocean. The shallow deep SAMW boundary in 2016, 2017, and 2020 (black line) and the relatively shallow MLs indicate that these are not core SAMW formation regions, though there is some ventilation and likely modification of SAMW properties. Red dots above (b) correspond to when the float was in the Pacific sector (red lines in panel a.).

**Table 1. Mean and standard deviation<sup>1</sup> of preformed properties in SAMW formation regions obtained from float observations**

Region	$\theta$ (°C)	Sal. (PSS-78)	[O <sub>2</sub> ] ( $\mu\text{mol kg}^{-1}$ )	[NO <sub>3</sub> <sup>-</sup> ] ( $\mu\text{mol kg}^{-1}$ )	[DIC] ( $\mu\text{mol kg}^{-1}$ )	$p\text{CO}_2$ ( $\mu\text{atm}$ )
Pacific	5.8 ± 0.6	34.2 ± 0.1	292 ± 6.2	21.5 ± 1.2	2135.1 ± 7.5	419.3 ± 14.4
Indian	9.3 ± 1	34.6 ± 0.2	271 ± 8.2	13.3 ± 2.9	2120 ± 6.3	404.4 ± 10.7

<sup>1</sup>Means and standard deviations are first calculated for each 0.05 kg m<sup>-3</sup> density bin, then a weighted average is calculated according to the SAMW volume fraction of each bin in the Pacific and Indian regions. The SD represents spatial and interannual variability in addition to measurement error.

297 Figures 3a and 3b). The relationship between potential density and each water property is nearly  
 298 identical between the Pacific and Indian formation regions, indicating that the preformed  
 299 property differences are primarily a function of the mean potential density of the waters formed  
 300 in each region (Figure S1). The relationship between density and ocean properties determined  
 301 from biogeochemical Argo observations show a generally good agreement with BSOSE for all  
 302 parameters except surface  $p\text{CO}_2$  (Figure 3, light dashed lines). Southern Ocean  $p\text{CO}_2$  and the  
 303 resulting air-sea flux is particularly hard for models to capture due to the non-linear relationship  
 304 between  $p\text{CO}_2$  and SST, DIC, and total alkalinity (Mongwe et al. 2018).

305 Despite capturing the overall relationship between biogeochemical properties and density  
 306 shown in Figure 3a, the mean BSOSE properties differ from the Argo observations in some  
 307 density classes. For instance, while BSOSE falls within the observed variability for oxygen,  
 308 nitrate, and DIC in the Pacific SAMW density range, in the Indian sector BSOSE oxygen and  
 309 nitrate are both higher than observations for the denser classes of SAMW. Direct comparison of  
 310 BSOSE sampled at float profile locations and float observed properties for winter waters with  
 311 deep (>200m) mixed layers within the regional SAMW density ranges indicates mean biases of -  
 312  $0.001 \pm 0.72$  °C,  $0.07 \pm 0.12$  salinity,  $-3.4 \pm 15.5$   $\mu\text{mol kg}^{-1}$  [O<sub>2</sub>],  $1.5 \pm 2.7$   $\mu\text{mol kg}^{-1}$  [NO<sub>3</sub><sup>-</sup>], and  
 313  $0.33 \pm 12.1$   $\mu\text{mol kg}^{-1}$  [DIC] in the Pacific and  $-0.47 \pm 1.19$  °C,  $-0.02 \pm 0.19$  salinity,  $2 \pm 12.6$   
 314  $\mu\text{mol kg}^{-1}$  [O<sub>2</sub>],  $-0.1 \pm 2$   $\mu\text{mol kg}^{-1}$  [NO<sub>3</sub><sup>-</sup>], and  $1.6 \pm 7.5$   $\mu\text{mol kg}^{-1}$  [DIC] in the Indian Ocean  
 315 (upper 200m average for MLs greater than 200m ± RMSE, Figure S2). The high RMSE for these  
 316 comparisons reflects the difficulty for a state estimate to exactly reproduce individual  
 317 observations, including differences in mixed layer depth at a specific location and the related  
 318 impact on ML properties. The mean biases are small relative to the magnitude of biogeochemical

319 property changes across the SAMW density range. Additionally, in this study we primarily use  
 320 BSOSE to explore interannual variability (Section 3.4), for which it is more important to  
 321 reproduce the large-scale density property relationships than to have perfect agreement between  
 322 every float profile and BSOSE output.

323 One of the few studies to characterize SAMW and the related AAIW properties in this  
 324 region used data from a cruise in the winter of 2005 (Carter et al. 2014) to determine deep winter  
 325 mixed layer properties for the SAMW that forms in the southeast Pacific. The SAMW formation  
 326 properties described in Carter et al. (2014) fall on the denser end of newly formed SAMW in the

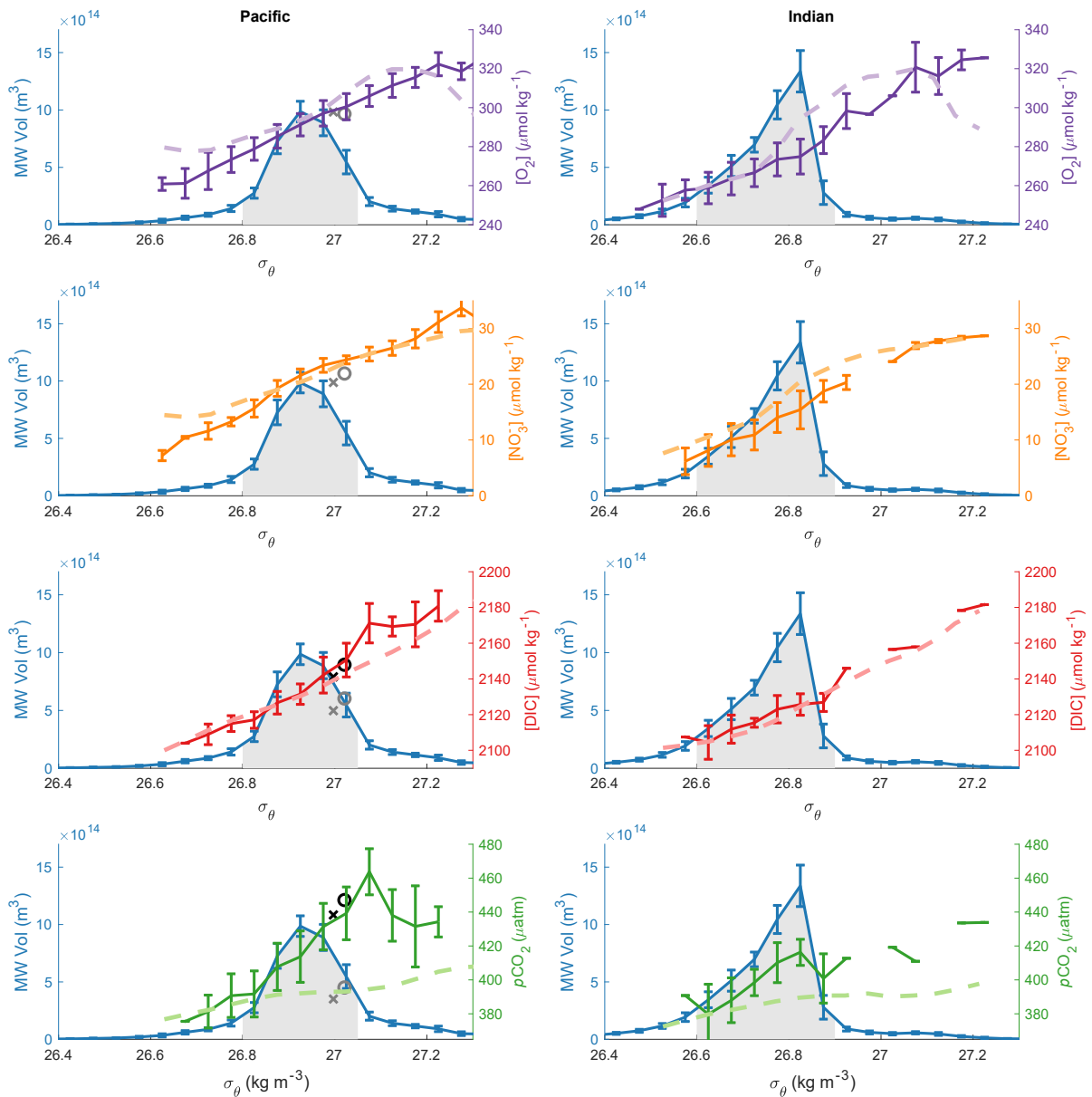




**Figure 3a (previous page). Mixed layer biogeochemical properties of SAMW during wintertime formation and SAMW volume.** Mode water volume and oxygen and nitrate, and estimated DIC and  $p\text{CO}_2$  are plotted as a function of potential density. The blue curves show the monthly mean volume of water within the ML that satisfies the low potential vorticity (PV) criteria  $PV < 40 \times 10^{-12} \text{ s}^{-1} \text{ m}^{-1}$ , obtained from the RG-Argo data set, for months August and September, 2005-2020, and binned into  $0.05 \text{ kg m}^{-3}$  wide density bins with the standard deviations indicating the interannual variability. The shaded areas under the volume curves indicates the density bins that contain at least 5% of SAMW by volume. Colored lines with error bars indicate the average properties  $\pm 1 \text{ SD}$  from biogeochemical floats, binned into the same  $0.05 \text{ kg m}^{-3}$  wide density bins. Volume and property data are from mixed layers that exceed 200 m. Dashed lines are the Aug-Sept mean biogeochemical properties from five-day averaged output from the Biogeochemical Southern Ocean State Estimate (BSOSE) and time averaged over years 2013-2019 where five-day averaged MLDs are deeper than 200m. Overlaid on the Pacific plots are markers indicating the SAMW formation properties identified in Carter et al. (2014) from their “North- Deep Mixed Layer Water” (northwest SAMW outcrop region, gray x’s) and “South-Deep Mixed Layer Water” (southeast SAMW outcrop region, gray o’s) samples. The Carter et al. (2014)  $[\text{NO}_3^-]$  is an average of  $2.9 \mu\text{mol kg}^{-1}$  lower than this study’s observations in the same density range. Adjusting the Carter et al. (2014) DIC and  $p\text{CO}_2$  for the equivalent difference in organic matter (plus change in alkalinity due to organic matter respiration and SST difference for  $p\text{CO}_2$ ) yields DIC and  $p\text{CO}_2$  shown by the black x’s and o’s. The longitude range of the Indian Ocean sector is  $68\text{--}170^\circ\text{E}$ , and the Pacific sector  $170\text{--}290^\circ\text{E}$ .

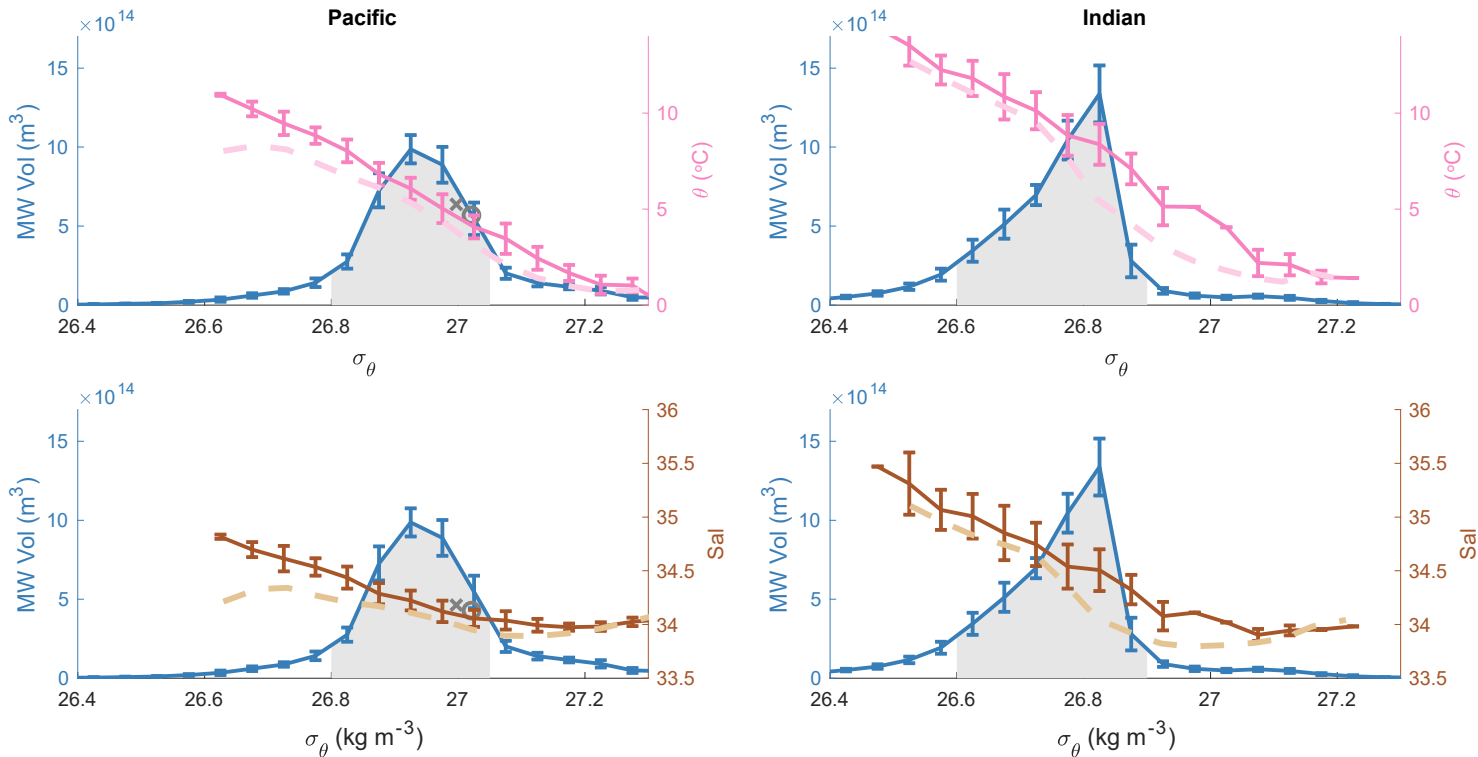


**Figure 3b. Equivalent to Fig 3a but for potential temperature and salinity.**

328 Pacific, as expected since the southeast Pacific SAMW is the coldest and freshest. The Carter et  
329 al. (2014) estimates are 0.9-1.4 °C colder and 0.05-0.01 PSU fresher than the mean Pacific  
330 SAMW properties described in this study. Samples of  $\theta$ , salinity, and  $[O_2]$  fall within  $\pm 1$  SD of  
331 the property-density relationships described in Figure 3a and 3b (gray symbols in Figure 3). The  
332 Carter et al. (2014)  $[NO_3^-]$  is  $\sim 2.9 \mu\text{mol kg}^{-1}$  lower than the  $[NO_3^-]$  observed in this study,  
333 indicating that either the SAMW formation region sampled in the present study has a greater  
334 fraction of older water with a stronger signal of respiration or that less biological production has  
335 occurred since that water has been at the surface, either of which could result in a higher  $[NO_3^-]$   
336 value. The  $[DIC]$  and  $pCO_2$  calculated from the Carter et al. (2014)  $[DIC]$  and alkalinity are  
337 correspondingly lower than observed values. Correcting for the different amount of biological  
338 activity using an assumed Redfield stoichiometry of 106C: 16N and recalculating the  $[DIC]$  and  
339  $pCO_2$  (in the latter case, also correcting for SST and the biological impacts on alkalinity) yields  
340 values that are within the uncertainty of our observed property relationships with density (Figure  
341 3, black symbols). This indicates that there is no fundamental disagreement between the  
342 carbonate system values derived from these float measurements and those observed by Carter et  
343 al. (2014). The  $[NO_3^-]$  and  $[DIC]$  differences between the Carter et al. (2014) results and the  
344 current study may additionally indicate variability or change on a multi-year time scale and  
345 warrants further exploration with longer time-series of observations or model output. The wide  
346 range of biogeochemical properties across the density range of newly formed SAMW illustrates  
347 the need for observations that span the entire density and spatial extent of newly formed SAMW  
348 to fully characterize properties at the time of formation.

349 Carter et al. (2021) used ocean observations and interior ocean mixing pathways to  
350 estimate preformed properties of oxygen, nitrate, silica, phosphate, and total alkalinity  
351 throughout the ocean interior. To compare Carter et al. (2021) to the current values for SAMW  
352 we applied the same geographic bounds for the Pacific and Indian regions to the Carter et al.  
353 (2021) preformed properties and masked results using the RG-Argo mean winter MLD criteria of  
354  $>200\text{m}$ . This yielded preformed properties at 200m depth of  $284.8 \pm 13.3 \mu\text{mol kg}^{-1} [O_2]$  and  
355  $22.3 \pm 3.9 \mu\text{mol kg}^{-1} [NO_3^-]$  in the Pacific and  $257.1 \pm 8.2 \mu\text{mol kg}^{-1} [O_2]$  and  $13.4 \pm 3.6 \mu\text{mol}$   
356  $\text{kg}^{-1} [NO_3^-]$  in the Indian Ocean (mean  $\pm 1$  SD). The differences in preformed  $[O_2]$  between  
357 Carter et al. (2021) and the current study are of a similar magnitude to our mean SAMW  
358 preformed oxygen undersaturation and therefore important to reconcile in future work.

359 Comparison between the results of Carter et al. (2021) and the current study is limited by the  
360 lack of density information from the Carter et al. (2021) results, so it is unclear whether the  
361 possible bias between these results is meaningful or an artifact of interpretation.

362 The relative properties of Pacific and Indian formation regions can be broadly interpreted  
363 using the property and density relationship described in Figure 3 as differences in mixing  
364 fraction of TW and AAIW/CDW in SAMW formation. The Indian SAMW formation region,  
365 which is located further north than the formation region in the Pacific, displays a greater  
366 influence of TW coming from the subtropics with higher temperatures and lower nutrients and  
367 carbon, whereas the Pacific SAMW formation region has a greater influence of upwelled deep  
368 water, with high carbon and nutrients, and cold temperatures. Oxygen concentrations follow the  
369 north-south temperature gradient, as oxygen air-sea exchange is fast relative to that of CO<sub>2</sub>,  
370 allowing the mixed layer to come close to solubility equilibrium with the atmosphere rather than  
371 being controlled by the initial [O<sub>2</sub>] of the mixing water masses. This interpretation that  
372 preformed biogeochemical properties are dependent on the mixing fraction is consistent with our  
373 physical understanding of how mode waters form in these two regions. An early analysis of the  
374 Southern Ocean State Estimate found SAMW forming in the Indian Ocean to have a greater  
375 fraction of volume transformed from the lighter (TW) waters than the SAMW forming in the  
376 Pacific (Cerovečki and Mazloff 2016). Using data from biogeochemical Argo floats, Fernández  
377 Castro et al. (2022) similarly documented the influence of salty, nutrient-poor subtropical waters  
378 on SAMW formation properties which decreases from the Indian to Pacific regions and is an  
379 important factor influencing the pre-formed nutrient content of SAMW.

380 The difference between the mean SAMW biogeochemical properties in the Indian and  
381 Pacific regions shown in Figure 3a indicates that, at a minimum, properties of newly formed  
382 SAMW will change depending on the relative volumes of water formed in the Pacific and Indian  
383 SAMW formation regions or within different density classes in the eastern and western areas of  
384 each region. During the Argo time period in both the Indian and Pacific sectors of the Southern  
385 Ocean, the SAMW volume trends showed a two-layer density structure, with an upper layer  
386 volume increase and a lower layer volume decrease (Kolodziejczyk et al. 2019; Portela et al.  
387 2020). The large range of properties within the SAMW density range in each of these two ocean  
388 sectors, shown in Figure 3, suggests that this SAMW volume variability is likely accompanied  
389 by similar variability of biogeochemical properties. Understanding the link between the density

390 of SAMW formed and the impact on subducted biogeochemical properties may be critical for  
 391 projection of future Southern Ocean conditions as the predicted poleward intensification of  
 392 Southern Ocean winds may impact mode water subduction rates differently in the Indian and  
 393 Pacific formation regions (Downes et al. 2017). While we now have sufficient data to describe  
 394 the mean SAMW formation properties in the Pacific and Indian Oceans, these basin-wide  
 395 averages likely mask the intra-basin differences and longer-term variability documented for the  
 396 physical properties. Current observational coverage alone is of insufficient density and length to  
 397 convincingly explore intra-basin biogeochemical differences.

398

### 399 3.2. Oxygen saturation during formation

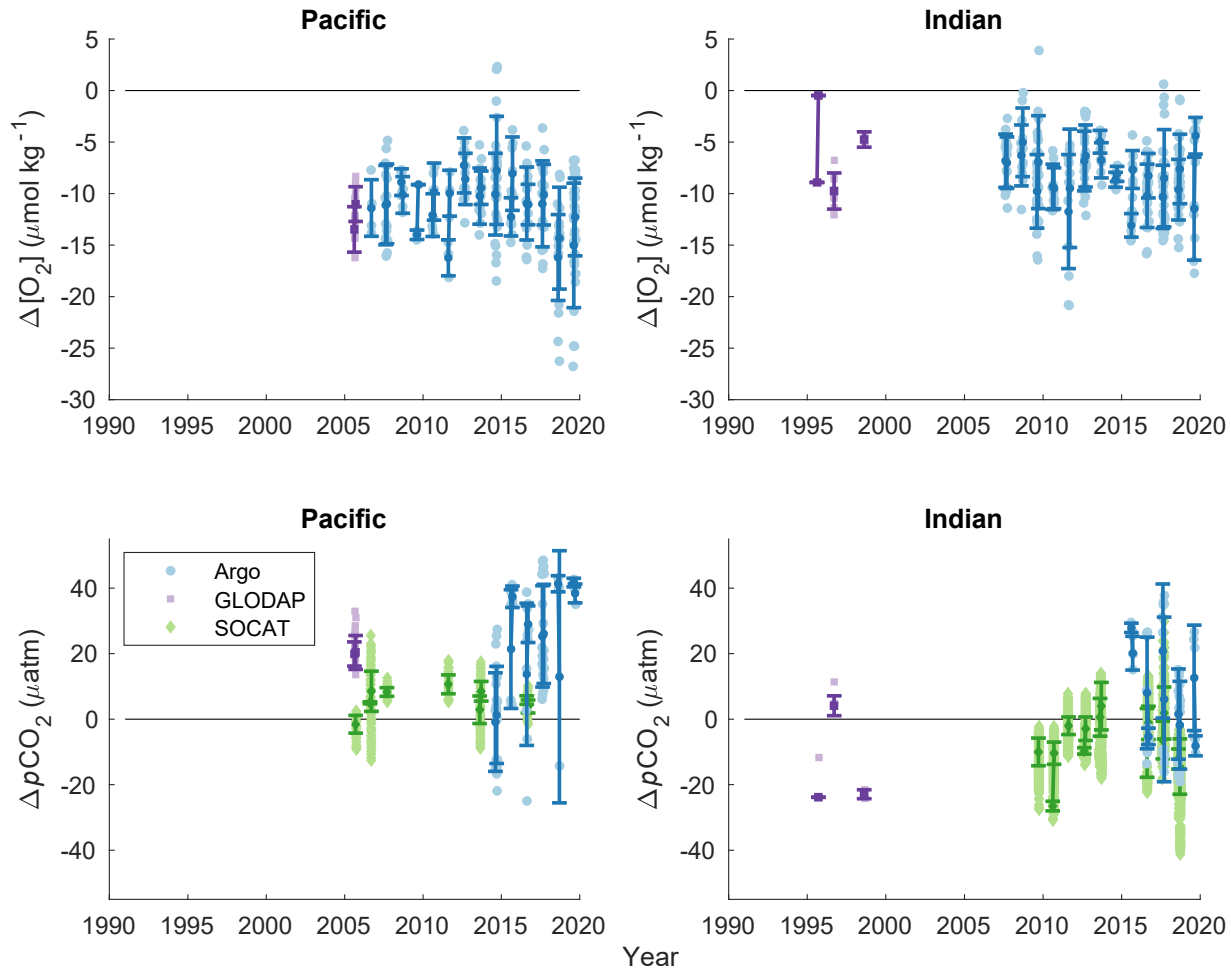
400 SAMW is undersaturated in oxygen at the time of formation in both the Pacific and  
 401 Indian formation regions (Table 2, Figure 4). Wintertime SAMW  $\Delta[O_2]$ , or the observed oxygen  
 402 concentration minus saturation concentration  
 403 ( $\Delta[O_2] = [O_2]_{\text{measured}} - [O_2]_{\text{saturation}}, \mu\text{mol kg}^{-1}$ ), is negative in almost all individual float  
 404 observations and in all August and September averages, consistent with the sparse observations  
 405 available in these wintertime locations in the GLODAP v2.2020 shipboard dataset. Pacific  
 406 SAMW has a mean  $\Delta[O_2]$  of  $-11.1 \pm 2.3 \mu\text{mol kg}^{-1}$  during formation and Indian SAMW has a  
 407 mean  $\Delta[O_2]$  of  $-7.7 \pm 2.7 \mu\text{mol}$

**Table 2. Mean  $\Delta[O_2]$  and  $\Delta pCO_2$  of SAMW at the time of formation**

Region	<sup>1</sup> $\Delta[O_2]$ ( $\mu\text{mol kg}^{-1}$ )			<sup>2</sup> $\Delta pCO_2$ ( $\mu\text{atm}$ )			
	Argo	GLODAP	Combined Argo & GLODAP	Argo	GLODAP	SOCAT	Combined Argo & SOCAT
<b>Pacific</b>	$-11.1 \pm 2.3$	$-12.2 \pm 1.7$	$-11.1 \pm 2.3$	$23.9 \pm 14.7$	$20.1 \pm 0.5$	$5.7 \pm 3.6$	$16.1 \pm 14.5$
<b>Indian</b>	$-7.9 \pm 2.4$	$-6 \pm 4.3$	$-7.7 \pm 2.7$	$9.3 \pm 11.7$	$-14 \pm 16.4$	$-6.4 \pm 7.5$	$0.1 \pm 12.2$

<sup>1</sup>  $\Delta[O_2] = [O_2]_{ML,observed} - [O_2]_{saturation}$ ;  $O_2$  saturation calculated as a function of temperature and salinity (Garcia and Gordon, 1992)

<sup>2</sup>  $\Delta pCO_2 = pCO_{2,surf} - X_{CO_2} \times (\frac{SLP}{1013.25} - pH_2O)$ ;  $X_{CO_2}$  from the NOAA Greenhouse Gas Marine Boundary Layer Reference (Dlugokencky et al. 2019), sea level pressure (SLP) in mbar,  $pH_2O$  calculated as a function of temperature and salinity (Zeebe and Wolf-Gladrow, 2001).



408

**Figure 4.  $\Delta p\text{CO}_2$  and  $\Delta[\text{O}_2]$  in SAMW formation regions from Argo floats and shipboard observations.** (Top row)  $\Delta[\text{O}_2]$  is calculated using the mixed layer average oxygen concentration from Argo floats (blue circles) and GLODAP shipboard measurements (purple squares) and is not corrected for local atmospheric pressure, reflecting the use of interior oxygen measurements relative to saturation concentration with an assumed atmospheric pressure of 1 atm. (Bottom row)  $\Delta p\text{CO}_2$  values from SOCAT  $p\text{CO}_2$  measurements (green diamonds), Argo ph-derived  $p\text{CO}_2$  estimates, and GLODAP DIC and alkalinity measurements using CO2SYS (van Heuven et al., 2011). SOCAT data are from near-surface underway systems, Argo data from the shallowest observation (typically 5-7m depth), and GLODAP data are from the upper 25m due to data availability.  $\Delta p\text{CO}_2$  for all data sources were calculated from NOAA ESRL atmospheric  $\text{CO}_2$  values, corrected for water vapor pressure, and a 2011-2020 climatological sea level pressure.  $\Delta p\text{CO}_2$  from Argo floats is higher (indicates more outgassing or less oceanic uptake) than recent SOCAT  $\Delta p\text{CO}_2$  but represents samples made over a wider range of SAMW waters.

409  $\text{kg}^{-1}$  (Table 2, average of float and GLODAP data). During the formation period, high winds  
410 drive strong gas exchange and an oxygen flux into the ocean to relieve undersaturation.  $\Delta[\text{O}_2]$  is  
411 calculated with an assumption of a standard sea level pressure (SLP) of 1013.25 mbar (1 atm).  
412 Wintertime SLP in the Southern Ocean is typically below 1013.25 mbar and accounting for the  
413 mean winter SLP in the Pacific and Indian formation regions would reduce oxygen  
414 undersaturation by  $\sim 30\%$  (Text S4). The fact that the waters stay undersaturated throughout the  
415 wintertime formation period indicates that a combination of surface cooling by atmospheric heat  
416 loss and continued entrainment of low oxygen sub-surface waters is maintaining undersaturation  
417 throughout the time of water mass formation and subduction.

418 Undersaturation of oxygen at the time of water mass formation has long been discussed  
419 as a source of error in interpreting interior ocean oxygen measurements but estimates of  
420 preformed oxygen undersaturation have primarily come from model results. Model results have  
421 indicated significant oxygen undersaturation during deep water formation in the North Atlantic  
422 and Southern Ocean (Ito et al. 2004; Duteil et al. 2013). The assumption that water masses are in  
423 equilibrium with atmospheric oxygen underpins one of the most common uses of interior ocean  
424 oxygen measurements, calculation of apparent oxygen utilization (AOU;  $\text{AOU} = [\text{O}_2]_{\text{saturation}} -$   
425  $[\text{O}_2]_{\text{measured}}$ ,  $\mu\text{mol kg}^{-1}$ ), where  $[\text{O}_2]_{\text{saturation}}$  is determined from temperature and salinity  
426 dependent oxygen solubility (García and Gordon 1992). This quantity is key to determining  
427 preformed quantities through the stoichiometric relationship between the consumption of oxygen  
428 and release of nutrients and DIC during respiration (e.g., Mackay and Watson 2021). Oxygen  
429 utilization rates (OUR) describe the average respiration in a parcel of water by combining  
430 apparent oxygen utilization (AOU) and an age tracer and, again, typically rely on the assumption  
431 that preformed oxygen is at saturation. While one study (Koeve and Kähler 2016) found that  
432 undersaturation in preformed oxygen did not make a large difference in calculated OUR due to  
433 other offsetting errors, this was based on a single model and did not have the observations to  
434 evaluate if that model accurately represented preformed biogeochemical properties.

435 The increasing number of oxygen-equipped profiling floats deployed throughout the  
436 ocean is enabling the first observational studies of wintertime oxygen saturation over large areas.  
437 The first basin-scale description of mixed layer  $\Delta[\text{O}_2]$  and air-sea oxygen fluxes over several  
438 years was also conducted in the Southern Ocean using Argo-oxygen floats, finding broad surface  
439 regions of undersaturated wintertime waters but without focusing on specific water masses or

440 ventilation regions (Bushinsky et al. 2017). In the Labrador Sea, Wolf et al. (2018) used Argo-  
441 oxygen floats to quantify significant undersaturation in Labrador Sea water at the time of  
442 formation that would bias AOU and derived biogeochemical properties. In the study that  
443 estimated preformed properties globally (Carter et al. 2021), errors in calculations of AOU were  
444 greatest in water formed in the Southern Ocean and in the North Pacific due to the strong degree  
445 of wintertime oxygen undersaturation in these regions. Broecker and Peng (1982) introduced the  
446 concept of True Oxygen Utilization (TOU), which is the difference between preformed oxygen  
447 concentration and the observed concentration, to account for the expected undersaturation during  
448 water formation events. Here we show for the first time in SAMW using direct observations of  
449 the wintertime formation that SAMW is undersaturated in oxygen when it leaves the ocean  
450 surface, altering the interpretation of observations in this water mass throughout the ocean  
451 interior and allowing for the calculation of TOU.

452         It is important to consider oxygen sensor accuracy and method of calibration when  
453 comparing to shipboard observations as some float oxygen data have been adjusted to match  
454 shipboard data. Oxygen data in the SOCCOM dataset (36 out of 53 floats) are calibrated using  
455 either atmospheric oxygen as a reference point or using initial shipboard casts if atmospheric  
456 data are not available (Johnson et al. 2017; Maurer et al. 2021). Deployments do not occur  
457 during the winter and these float oxygen data are therefore independent of the GLODAP  
458 shipboard data presented in Figure 4 and Table 2. Oxygen data in the UW Argo O<sub>2</sub> dataset are  
459 re-processed using a two-point correction (one near-surface and one deep calibration value). The  
460 near-surface values are air measurements (if available) or World Ocean Database (WOD, Garcia  
461 et al. 2010) mean values. Surface reference values for the WOD were only used if the water was  
462 close to saturation (98-101% O<sub>2</sub> saturation). It is therefore unlikely that any of the shipboard  
463 observations shown in Figure 4 were used in the calibration. Therefore, while the uncertainty of  
464 oxygen data corrected to WOD is higher than air-calibrated data, these also represent  
465 independent observations from the GLODAP data. Uncertainties for the SOCCOM (1-2  $\mu\text{mol}$   
466  $\text{kg}^{-1}$ ) and UW Argo O<sub>2</sub> ( $\sim 3 \mu\text{mol kg}^{-1}$ ) datasets are much smaller than the mean offset and SD of  
467 the data shown here and are therefore unlikely to be a major factor in the undersaturation found  
468 in the pre-formed oxygen estimates.

469

470

471

472 **3.3 Carbon dioxide saturation during formation**

473 Mean monthly derived  $\Delta p\text{CO}_2$  (surface  $p\text{CO}_2$  minus atmospheric  $p\text{CO}_2$ , Text S2)  
474 determined only from float observations is positive in the Pacific ( $22.5 \pm 13.5 \mu\text{atm}$ ) formation  
475 region and slightly positive in the Indian SAMW formation region ( $9.5 \pm 12.9 \mu\text{atm}$ ) (Table 2;  
476 Figure 4, bottom). In both the Pacific and Indian SAMW formation regions the  $\Delta p\text{CO}_2$   
477 calculated from float observations overlaps with, but is generally higher than, either direct  
478 shipboard measurements (SOCAT) or derived  $\Delta p\text{CO}_2$  from paired DIC and alkalinity  
479 measurements (GLODAP). SOCAT  $p\text{CO}_2$  observations are direct measurements with accuracy  
480 better than  $5 \mu\text{atm}$  (including quality flags A-D, Lauvset et al. 2017), while the float-derived  
481  $p\text{CO}_2$  estimates utilize a recently developed technique with a theoretical uncertainty of  
482 approximately  $\pm 11 \mu\text{atm}$  (Williams et al. 2017). Float observations have previously shown  
483 higher  $p\text{CO}_2$  during the winter than has been recorded in the SOCAT database (Gray et al. 2018;  
484 Williams et al. 2018). This elevated wintertime  $p\text{CO}_2$  yields a reduction in the Southern Ocean  
485 (south of  $35^\circ\text{S}$ )  $\text{CO}_2$  sink in 2015-2017 from  $1.1 \text{ Pg C yr}^{-1}$  based on SOCAT data alone to  $0.75$   
486  $\text{Pg C yr}^{-1}$  using a combined SOCAT and SOCCOM dataset (Bushinsky et al. 2019). These results  
487 have been challenged, most recently by a study using atmospheric  $\text{CO}_2$  measurements and  
488 atmospheric transport models to constrain the Southern Ocean sink (Long et al. 2021), which  
489 yielded a stronger Southern Ocean  $\text{CO}_2$  sink, though with overlapping uncertainties between the  
490 atmospheric constraint and the SOCCOM and SOCAT float-based  $p\text{CO}_2$  estimates in all months  
491 for which atmospheric data existed and potential complications from previously documented  
492 interannual and decadal variability.

493 The key question for average values of  $\Delta p\text{CO}_2$  or air-sea fluxes is whether averaged float  
494 estimates of  $p\text{CO}_2$  are accurate, not whether individual observations are precise. Crossover  
495 comparisons between ship and float  $p\text{CO}_2$  have indicated a possible high bias of float  $p\text{CO}_2$  by  
496  $\sim 4 \mu\text{atm}$  (Fay et al. 2018; Gray et al. 2018; Williams et al. 2018), smaller than the differences  
497 between the Argo and SOCAT mean values in Table 2. An updated crossover comparison with  
498 the addition of a filter eliminating crossover density differences  $> 0.03 \text{ kg m}^{-3}$  yields a mean float-  
499 derived  $p\text{CO}_2$  bias of  $-1.86 \pm 15.8 \mu\text{atm}$  (SOCAT minus floats,  $n = 52$ , Supplemental Figure S3).  
500 Recent work evaluating float  $p\text{CO}_2$  against shipboard observations indicates that float  $p\text{CO}_2$  may  
501 be high by  $\sim 6 \mu\text{atm}$  (Mackay and Watson 2021; Wu et al. 2022) and comparison against aircraft-



502 derived CO<sub>2</sub> fluxes indicate that float-derived outgassing is too strong in the winter due to high-  
503 biased  $p\text{CO}_2$  values. This makes it unlikely that an error in the  $p\text{CO}_2$  estimation method is  
504 responsible for the entire 17-20  $\mu\text{atm}$  difference in  $\Delta p\text{CO}_2$  between the mean Argo and SOCAT  
505 values shown in Fig. 4, though it may be responsible for some of the offset.

506 A large portion of the difference between the SAMW formation  $\Delta p\text{CO}_2$  from SOCAT  
507 and Argo is more likely due to the differences in sample distribution within each of these  
508 formation regions. The strong coupling of density and biogeochemical properties seen in Figure  
509 3 highlights the importance of sampling the full range of densities. Previous work demonstrating  
510 spatial variability in physical formation properties of SAMW indicates that spatial variations in  
511 biogeochemical properties are also likely to exist. Histograms of the relative frequency of  
512  $\Delta p\text{CO}_2$ , longitude,  $\sigma_\theta$ , and  $\theta$  of mode water formation region observations by the Argo and  
513 SOCAT datasets identify differences in the sample distributions of these observations (Figure 5).  
514 In the Pacific, SOCAT-determined  $\Delta p\text{CO}_2$  has a peak of  $\sim 0$   $\mu\text{atm}$  and a tail toward positive  
515 values. The SOCAT observations are primarily from  $\sim 170^\circ\text{E}$ , at the very western edge of the  
516 Pacific basin, while one cruise crossed the Pacific in 2006. This results in observations that are  
517 primarily from  $\sigma_\theta$  26.88 – 26.9  $\text{kg m}^{-3}$  and  $\theta$  of 7.26 – 7.94  $^\circ\text{C}$ . Float observations cover a  
518 broader range of locations within the Pacific and are consequently spread more evenly across the  
519 SAMW density range. SOCAT sample coverage in the Indian Ocean is primarily from cruises  
520 originating from Tasmania and do not cover the large formation regions in the central and  
521 western Indian Ocean. There are relatively few GLODAP-derived  $\Delta p\text{CO}_2$  values in either basin,  
522 so our best estimate of the  $\Delta p\text{CO}_2$  for each region is an average of monthly values from the  
523 SOCAT and Argo datasets, yielding  $16.1 \pm 14.5$   $\mu\text{atm}$   $\Delta p\text{CO}_2$  in the Pacific and  $0.1 \pm 12.2$   $\mu\text{atm}$   
524  $\Delta p\text{CO}_2$  in the Indian Ocean. If we applied a uniform 6  $\mu\text{atm}$  bias to the float-derived  $p\text{CO}_2$   
525 values, it would lower the mean  $\Delta p\text{CO}_2$  at formation to  $12.7 \pm 12.8$   $\mu\text{atm}$  in the Pacific and  $-3.1$   
526  $\pm 10.7$   $\mu\text{atm}$  in the Indian Ocean.

527 The entire Southern Ocean is a significant sink for contemporary carbon, mainly driven  
528 by the increase in atmospheric anthropogenic carbon and resulting oceanic anthropogenic uptake  
529 (Mikaloff Fletcher et al. 2006; Gruber et al. 2009b; DeVries 2014). Much of this anthropogenic  
530 carbon is both stored in and exported by mode and intermediate waters (Sabine et al. 2004;  
531 Mikaloff Fletcher et al. 2006; Álvarez et al. 2009; Gruber et al. 2009a; Sabine and Tanhua 2010).  
532 Model-derived calculations of anthropogenic carbon uptake use the difference in ocean carbon

533 fluxes and accumulation between model runs that do and do not include increasing atmospheric  
534 carbon to determine uptake rates of anthropogenic carbon (Iudicone et al. 2011, 2016;  
535 Groeskamp

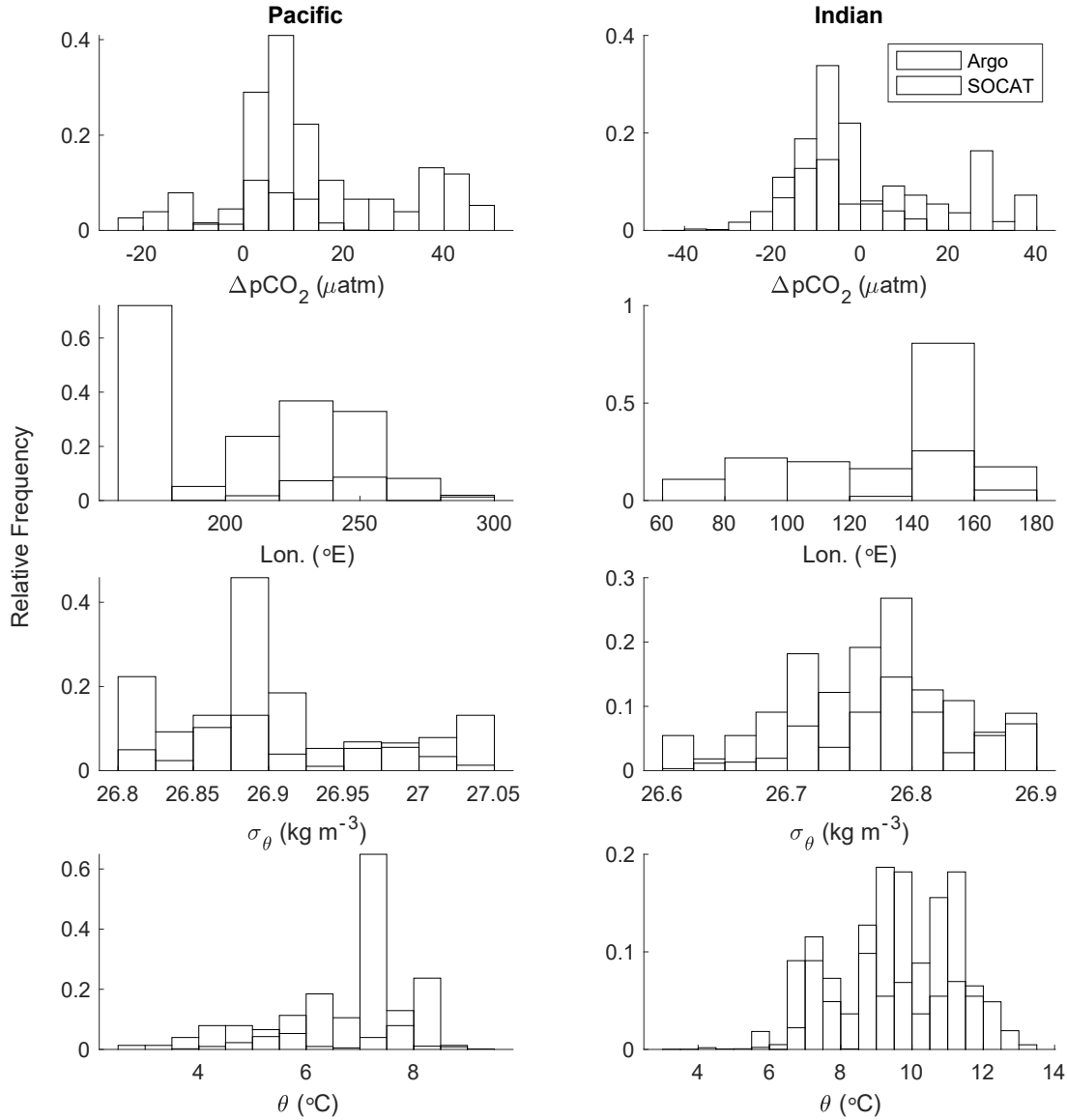


**Figure 5. Properties associated with  $\Delta p\text{CO}_2$  calculated from SOCAT and Argo.** Relative frequency histograms of calculated  $\Delta p\text{CO}_2$  and the associated longitude, potential density, and potential temperature for SAMW formation properties in the Pacific and Indian Oceans. SOCAT  $\Delta p\text{CO}_2$  values are primarily from narrow geographic regions in the Pacific sector near New Zealand and in the Indian sector near Tasmania. Biogeochemical Argo data are spread across the sectors, with more distributed density and potential temperature values as well.  $\Delta p\text{CO}_2$  for SOCAT is similarly within relatively narrow ranges for both sectors, while Argo-derived  $\Delta p\text{CO}_2$  overlaps with and, on average, is higher than SOCAT  $\Delta p\text{CO}_2$ . GLODAP-derived  $\Delta p\text{CO}_2$  and associated properties are not shown, as they represent a much smaller sample range and were not included in the property averages (Table 2).

537 et al. 2016). This approach relies on an accurate representation of water mass properties and the  
538 physical and biogeochemical processes that influence the carbonate system in models, which  
539 have been shown to have difficulty in capturing the seasonal cycle of  $p\text{CO}_2$  and air-sea  $\text{CO}_2$   
540 fluxes in the Southern Ocean (Mongwe et al. 2018). If the models do not accurately capture  
541 contemporary carbon uptake, then the anthropogenic carbon fluxes and storage will be biased.

542 Recent work attempting to constrain the magnitude of wintertime outgassing in the  
543 Southern Ocean (Gray et al. 2018; Bushinsky et al. 2019; Mackay and Watson 2021; Sutton et al.  
544 2021; Long et al. 2021) makes it all the more important to understand the mechanisms that could  
545 contribute to total Southern Ocean uptake of contemporary and anthropogenic carbon. A  $\Delta p\text{CO}_2$   
546 during formation that is near or above zero indicates that SAMW does not contribute to the total  
547 Southern Ocean contemporary carbon uptake during formation. Given the increase in  
548 atmospheric  $p\text{CO}_2$  from anthropogenic emissions, it is likely that these waters would have been a  
549 pre-industrial source of carbon to the atmosphere and the current near-zero  $\Delta p\text{CO}_2$  represents an  
550 anthropogenic carbon sink. It is clear from observed accumulation of anthropogenic carbon in  
551 the ocean interior (Sabine et al. 2004; Mikaloff Fletcher et al. 2006; Sabine and Tanhua 2010;  
552 Gruber et al. 2019a) that SAMW is important for the storage of anthropogenic carbon and export  
553 to the ocean interior, but the modeling work that has sought to elucidate whether SAMW  
554 accumulates anthropogenic carbon through surface or interior processes has not had robust  
555 observations for validation (Iudicone et al. 2011; Groeskamp et al. 2016). Here we provide both  
556 the mean biogeochemical properties and their distribution with respect to water mass density that  
557 can be used to validate model property distributions and representation of contemporary carbon  
558 fluxes, thereby improving future estimates of the magnitude and mechanisms of anthropogenic  
559 carbon uptake and partitioning of uptake between surface and interior processes.

560

### 561 **3.4 Spatial and interannual variability of SAMW formation properties**

562 Almost 15 years of Argo observations have provided invaluable information about strong  
563 interannual and spatial variability of SAMW physical properties. Argo observations have  
564 revealed that the strong wintertime MLD anomalies in the Pacific, Indian, and Atlantic sectors  
565 that develop in some years, and are associated with SAM and ENSO, tend to be out of phase in  
566 the western and eastern parts of ocean sectors (Meijers et al. 2019; Tamsitt et al. 2020; Cerovečki  
567 and Meijers 2021). In years with anomalously strong formation of colder and denser varieties of

568 SAMW in the eastern parts of the Indian and Pacific sectors, the formation of warmer and lighter  
569 varieties of SAMW in the western part of both ocean sectors is anomalously weak, enhancing the  
570 net cooling and densification in each ocean sector. Conditions reverse in years with the  
571 preferential formation of warmer and lighter varieties of SAMW (Cerovečki and Meijers 2021).  
572 Anomalies that develop in the western part of one ocean sector can subsequently be advected by  
573 the ACC to arrive approximately one year later to the eastern SAMW formation region of the  
574 same ocean sector (Meijers et al. 2019; Cerovečki et al. 2019). This pattern of an east-west  
575 dipole in MLD anomalies and propagation of strong anomalies is evident in the BSOSE Aug-  
576 Sept time-mean MLD (Figure 6). During the 2013-2019 period of BSOSE model simulation  
577 analyzed here, the strongest MLD anomalies developed in 2016 when a strong El Niño event  
578 coincided with a strong positive SAM early in the year (Figure 6a). By austral winter 2016, both  
579 indexes transitioned to strongly negative (Meijers et al. 2019). The in-phase atmospheric modes  
580 resulted in anomalously deep and cold wintertime mixed layers in the central Pacific, and  
581 anomalously shallow and warm mixed layers in the southeast Pacific (Meijers et al. 2019;  
582 Cerovečki et al. 2019).

583 In addition to the previously described temperature anomalies (not shown) associated  
584 with the 2016 MLD anomalies, BSOSE displays high DIC and high  $\text{NO}_3^-$  in the central Pacific  
585 and low DIC and  $\text{NO}_3^-$  in the eastern Pacific (Figure 6b). The opposite pattern is observed in  
586 2015, when anomalously shallow MLs in the central Pacific were associated with low DIC and  
587 low  $\text{NO}_3^-$ , while anomalously deep MLs in the eastern Pacific entrained high DIC and  $\text{NO}_3^-$   
588 waters. These anomaly maps suggest a link between SAM, ENSO, and biogeochemical  
589 anomalies, but the BSOSE time series is too short for more definitive attribution in the current  
590 study. Due this relatively short time period we chose to investigate interannual winter property  
591 anomalies rather than e.g. carrying out an EOF analysis, though an initial EOF analysis produced  
592 qualitatively similar results.

593 A time-series of the wintertime (Aug-Sept) mean ML property anomalies within the  
594 Pacific SAMW density range ( $26.8 \leq \sigma_\theta < 27.05 \text{ kg m}^{-3}$ ) considered separately in the central (45-  
595 64°S, 170-246°E) and southeast (45-64°S, 246-290°E) Pacific reveals a similar dipole pattern of  
596 DIC, nitrate, and oxygen as found in prior work considering physical properties (Figure 7).  
597 These two regions of the Pacific are not entirely out of phase, as the biogeochemical properties  
598 during the formation time period are not only governed by the local surface forcing that drives

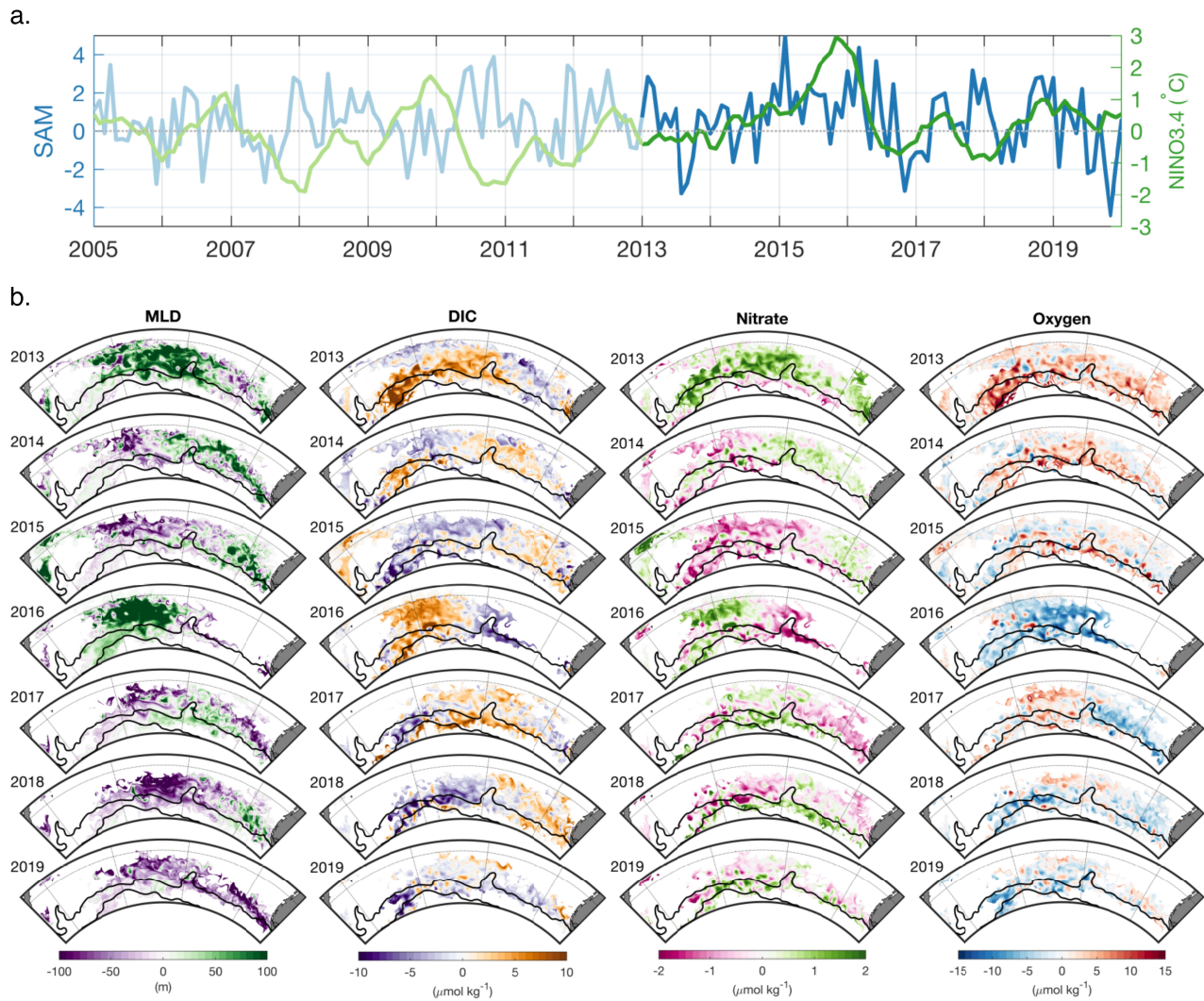


**Figure 6. Time series of ENSO, SAM, and BSOSE winter anomalies in MLD, DIC, nitrate, and oxygen.** (a) SAM (blue) and ENSO (green) indices are highlighted during the years covered by BSOSE. (b) Winter (Aug-Sept) anomalies for MLD, DIC, nitrate, and oxygen demonstrate the combined influence of ENSO and SAM. Years and regions with deep MLD anomalies (green) are associated with higher DIC (orange) and nitrate (green). Spatial patterns of anomalies demonstrate a dipole between the central Pacific and southeast Pacific in many years, similar to a previously demonstrated pattern in SST, and Salinity (Cerovečki and Meijers, 2021).

599 MLD anomalies, but also the properties from water formed in prior years incorporated through  
 600 entrainment and lateral induction. The mean property anomalies of the Pacific are more closely  
 601 correlated with central Pacific than the southeast Pacific due to the larger volume of water  
 602 formed in the central Pacific, in agreement with observational work by Cerovečki and Meijers  
 603 (2021).

604           Oxygen time variability is more complicated than that of nitrate and DIC, as the fast gas  
605 exchange rate moves to restore air-sea equilibrium and replenish waters that are initially  
606 deficient in oxygen but have low temperatures and high solubility. In some years, such as 2016  
607 when the strong El Niño and strongly positive SAM combined to produce anomalously deep  
608 MLs in the central Pacific, the oxygen anomaly is negative, indicating that the entrainment signal  
609 was strong and persisted through the SAMW formation period (Figs. 6 and 7). In other years,  
610 such as 2013, deep MLs in the central Pacific are associated with positive oxygen anomalies.  
611 This dichotomy reflects the competing processes that impact oxygen in the upper ocean. In years  
612 with strong heat loss to the atmosphere, cooler temperatures will increase the solubility, which,

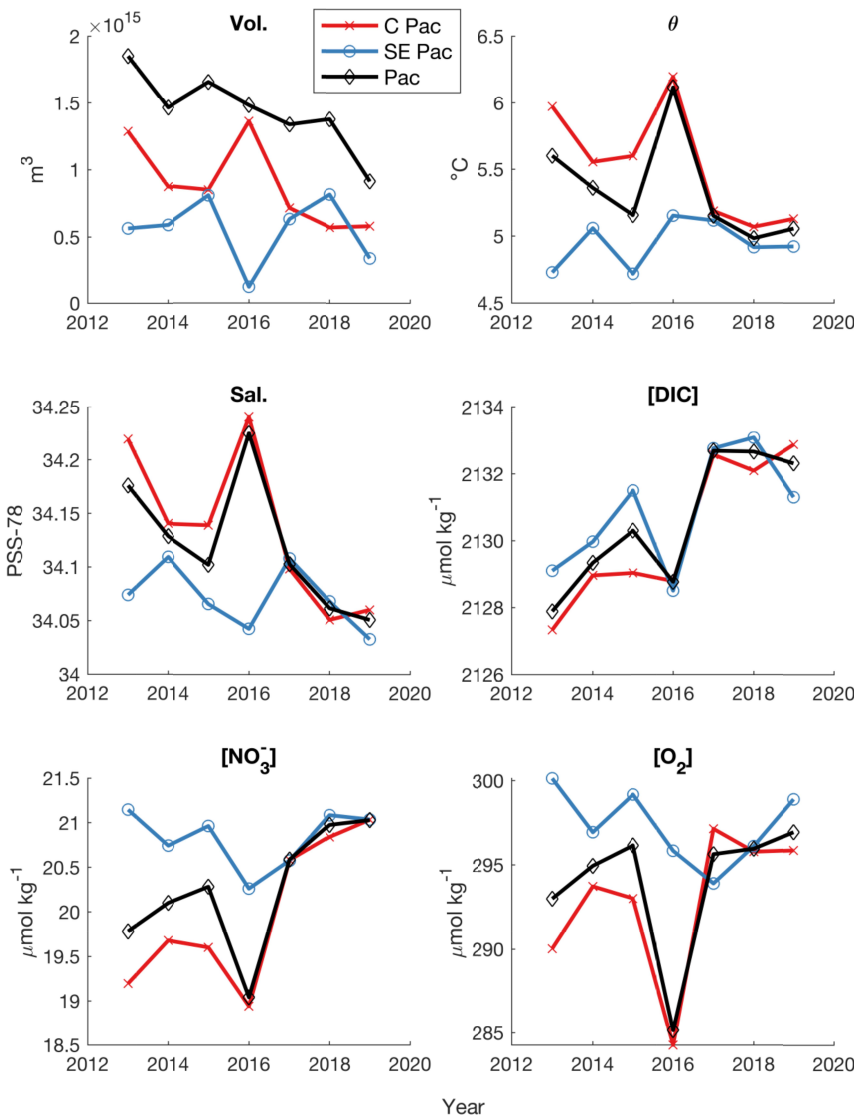


**Figure 7. SAMW Pacific formation properties in BSOE.** Anomalies are mean winter (Aug-Sept) ML properties in the Pacific SAMW density range ( $26.8 \leq \sigma_{\theta} < 27.05 \text{ kg m}^{-3}$ ). Anomalies are calculated for the central (red line, 45-64°S, 170-246°E), southeast (blue, 45-64°S, 246-290°E), and overall Pacific (black, 45-64°S, 170-290°E) regions.

613 coupled with strong winds driving high air-sea gas exchange rates, will tend to increase the  
 614 oxygen concentration in the surface ocean. On the other hand, deeper mixing will entrain more  
 615 low-oxygen water from below and the increased volume of the mixed layer will slow the change  
 616 in oxygen concentration for a given air-sea flux. Years with reduced air-sea heat loss in the  
 617 winter and shallower MLs are characterized by warmer temperatures and lower solubility but  
 618 also less entrainment of low-oxygen waters. A plot of SAMW oxygen concentration against  
 619 potential temperature for the Pacific and Pacific sub-regions reveals that the main signal is a  
 620 fairly consistent offset relative to oxygen saturation of which approximately 1/3 is due to low  
 621 SLP (Figure S4), implying that not only do oxygen concentrations closely follow interannual



622 temperature changes, but also that the balance of the above processes leads to a consistent  $\Delta[\text{O}_2]$   
623 despite large changes in MLD and temperature. Both the magnitude of the  $\Delta[\text{O}_2]$  offset and the  
624 lack of variability in BSOSE are consistent with float and ship-board observations (Figure 4).  
625 (Wolf et al. 2018)

626 Interestingly, the differences in biogeochemical property anomalies observed between the  
627 central and southeastern Pacific are more pronounced during the first half of the BSOSE time  
628 series than after 2016 (Figure 7). Physical and biogeochemical properties across the Pacific  
629 become more uniform after the 2016 El Niño and remain so through 2017, 2018, and 2019  
630 (Figure 7, difference between the central Pacific (red line, 45-64°S, 170-246°E), and southeast  
631 Pacific (blue line, 45-64°S, 246-290°E)). This is likely caused in part by advection of anomalies  
632 from the central to southeast Pacific following the strong 2016 El Niño, as previously shown for  
633 temperature anomalies using Argo data (Cerovečki and Meijers 2021). Similar advection of  
634 anomalies of biogeochemical properties from west to east Pacific SAMW formation regions is  
635 evident in Figure 6. This propagation of signals across the entire Pacific formation region is  
636 suggested by the apparent movement of anomalies from west to east in Figure 6. Advection of  
637 biogeochemical anomalies in BSOSE is more prominent when viewed in a Hovmöller diagram  
638 of the volume-weighted average upper ocean anomalies in the region where Aug-Sept MLs  
639 exceed 150m (Figure S5). Similar advective signals have been described in Argo observations of  
640 physical properties (Cerovečki and Meijers 2021) and previously in modeled temperature,  
641 salinity, and air-sea fluxes of oxygen and carbon dioxide (Verdy et al. 2007).

642 We are left with a framework where interannual variability in the biogeochemical  
643 properties of newly formed SAMW is influenced by a mix of local atmospheric forcing  
644 combined with the lateral induction of prior signals into the wintertime mixed layer. This mix of  
645 processes agrees with prior work on SAMW physical properties (Meijers et al. 2019; Cerovečki  
646 et al. 2019; Li et al. 2021) and a study demonstrating that surface fluxes are often not strong  
647 enough to change the physical properties of SAMW, due to the memory in the large volume of  
648 sub-surface water (Rintoul and England 2002). Advective propagation of anomalies can  
649 sometimes be interrupted by sufficiently large forcing events, but many biogeochemical  
650 anomalies do transit the entire Pacific SAMW formation region (Figure S5).

651

#### 652 **4. Conclusions**

653 Here we use biogeochemical Argo float observations spanning a seven-year period to  
654 characterize for the first time the regional distribution of SAMW formation properties in the  
655 Pacific and Indian sectors, finding that the colder, fresher SAMW that forms in the Pacific is also  
656 higher in oxygen, nitrate, DIC, and  $p\text{CO}_2$  than SAMW that forms in the Indian Ocean. The  
657 differences in formation properties between the Pacific and Indian Oceans reflect the density of  
658 SAMW formed in each region. The distribution of wintertime properties against density is  
659 consistent in both sectors, indicating that these property distributions predominantly represent a  
660 continuum of source water mass mixing between thermocline water, upwelled circumpolar deep  
661 water, AAIW, and re-entrained SAMW.

662 In both the Pacific and Indian sectors, SAMW is undersaturated in oxygen at the time of  
663 formation, with slightly stronger undersaturation present in the Pacific formation regions. This  
664 undersaturation must be taken into account when calculating derived quantities that normally  
665 assume oxygen saturation at the time of water mass formation. This observed undersaturation  
666 appears fairly constant over the observed time period and matches results from biogeochemical  
667 ocean state estimate BSOSE that suggest some consistent balance between undersaturation due  
668 to cooling or entrainment and replenishment by air-sea gas exchange that is maintained despite  
669 large interannual differences in oxygen concentration and SST.

670 There are large differences between the mean  $\Delta p\text{CO}_2$  of newly formed SAMW estimated  
671 from profiling floats and that measured by underway shipboard observations. Float estimates of  
672 winter  $\Delta p\text{CO}_2$  are on average  $\sim 17$   $\mu\text{atm}$  higher in this study than the limited SOCAT  
673 observations from the same formation regions, part of which could be due to a systemic bias in  
674 float-derived  $p\text{CO}_2$ . However, float observations are geographically more uniformly distributed  
675 over the SAMW formation regions, sampling a wider range of properties than has been measured  
676 from shipboard observations. The bulk of these differences can be explained by the different  
677 sample distribution in the two datasets. During the wintertime formation period, SAMW has a  
678 positive  $\Delta p\text{CO}_2$  (average of SOCAT and float datasets) in the Pacific and a near neutral  $\Delta p\text{CO}_2$   
679 in the Indian formation region. This indicates that SAMW formation is not directly driving air-  
680 sea uptake of contemporary  $\text{CO}_2$ . The biogeochemical observations here provide for the first  
681 time the comparison data necessary to determine if models used to understand how  
682 anthropogenic carbon enters the ocean interior through mode and intermediate waters are  
683 accurately representing ocean biogeochemistry during mode water formation.

684           There are sufficient float biogeochemical observations to constrain mean wintertime  
685 formation properties but there are not currently enough to investigate sub-regional or interannual  
686 variability. We thus used BSOSE output to explore spatial and temporal SAMW variability,  
687 focusing on the Pacific SAMW formation region. In the Pacific the link between climate modes  
688 of variability and SAMW response is the strongest and BSOSE representation of the spatial  
689 distribution of deep winter mixing in the Pacific was more similar to these from the RG-Argo  
690 than in the Indian sector. Comparison between this study and Cerovečki and Meijers (2021)  
691 indicates that BSOSE well reproduces the large-scale response of the MLD to SAM and ENSO,  
692 showing the dipole pattern of variability between the central and southeast Pacific. BSOSE also  
693 accurately represents the relationships between biogeochemical properties and water mass  
694 density that we find in observations, giving good confidence that it can be used to develop our  
695 understanding of the link between climate forcing and biogeochemical property variability in  
696 SAMW formation waters.

697           Interannual variability in the central and southeast Pacific biogeochemical formation  
698 properties display a see-saw pattern similar to that previously found in observations of physical  
699 properties. The suggested dipole pattern of biogeochemical properties relates well to the  
700 corresponding pattern in mixed layer depth and entrainment of deeper waters, with high nitrate  
701 and high DIC in regions and years with deep mixed layer anomalies and low nitrate and low DIC  
702 when the mixed layer is anomalously shallow. We expect that with more biogeochemical  
703 observations made in the Southern Ocean, these patterns will become evident in the observations  
704 as well. Interannual variability in oxygen concentration closely follows changes in ML  
705 temperature with a consistent undersaturation indicating that ML waters do not have time to  
706 equilibrate with the atmosphere regardless of whether the MLDs are anomalously deep or  
707 shallow.

708           Future work should focus on decomposing interannual variability in biogeochemical  
709 signals between those driven by local forcing and the influence of multi-year advective signals.  
710 A detailed understanding of the variability present in SAMW formation regions will help to  
711 understand how sensitive the interior volume is to changes in volume and properties of the  
712 individual formation regions and how strongly those variations are either modulated by the total  
713 interior SAMW volume or transported to the rest of the ocean.

714 SAMW is a critical water mass for the uptake of anthropogenic carbon and transport of  
 715 oxygen and nutrients into the ocean interior. Improving our understanding of SAMW  
 716 biogeochemical properties and their variability is of fundamental importance for improving our  
 717 interpretation of interior ocean measurements, providing better validation for models, and  
 718 therefore enabling new understanding of how SAMW functions in these global biogeochemical  
 719 cycles.

720

721 **Acknowledgements:**

722 Float data were collected and made freely available by the Southern Ocean Carbon and Climate  
 723 Observations and Modeling (SOCCOM) Project funded by the National Science Foundation,  
 724 Division of Polar Programs (NSF PLR -1425989 and OPP-1936222), supplemented by NASA,  
 725 and by the International Argo Program and the NOAA programs that contribute to it. The Argo  
 726 Program is part of the Global Ocean Observing System. The Surface Ocean CO<sub>2</sub> Atlas (SOCAT)  
 727 is an international effort, endorsed by the International Ocean Carbon Coordination Project  
 728 (IOCCP), the Surface Ocean Lower Atmosphere Study (SOLAS) and the Integrated Marine  
 729 Biosphere Research (IMBeR) program, to deliver a uniformly quality-controlled surface ocean  
 730 CO<sub>2</sub> database. The many researchers and funding agencies responsible for the collection of data  
 731 and quality control are thanked for their contributions to SOCAT. The specific SOCAT data used  
 732 in this study were contributed by PIs K. Currie, A. Sutton, T. Trull, C. Sabine, T. Takahashi, C.  
 733 Sweeney, S. C. Sutherland, T. Newberger, D. R. Munro, B. Tilbrook, J. Akl, and C. Neill.  
 734 SOCAT data from the R/V Tangaroa were collected by the National Institute of Water and  
 735 Atmospheric Research (funded by the New Zealand Ministry of Business, Innovation and  
 736 Employment). SOCAT data from the R/V Gould and R/V Palmer were funded by the National  
 737 Oceanic and Atmospheric Administration through the Global Ocean Monitoring and Observing  
 738 Program and the Office of Oceanic and Atmospheric Research and by the National Science  
 739 Foundation (grant numbers PLR 1341647 and 1543457). SOCAT underway data from Tilbrook,  
 740 Akl and Neill were sourced through Australia's Integrated Marine Observing System (IMOS) –  
 741 IMOS is enabled by the National Collaborative Research Infrastructure Strategy (NCRIS).  
 742 Specific GLODAP data were collected on the R/Vs Knorr, Aurora Australis, Malcolm Baldrige,  
 743 and M.-Dufresne. SMB was supported by NASA grants NNX17AI73G and 80NSSC22K0156  
 744 and benefited from support by the NOAA Climate Program Office's Climate Observations and

745 Monitoring, Climate Variability and Predictability, and Global Ocean Monitoring and  
746 Observation programs (NA21OAR4310260). IC was supported by NASA grants  
747 80NSSC22K0156 and 80NSSC19K1115. This is SOEST contribution XXXX.

748

#### 749 **Conflict of Interest Statement**

750 The authors have no conflicts of interest to declare.

751

#### 752 **Open Research**

753 Datasets used in this paper are from these references and the associated repositories:

754 Biogeochemical float data are from the May 2021 SOCCOM snapshot (Johnson et al,  
755 2017; [doi.org/10.6075/J0T43SZG](https://doi.org/10.6075/J0T43SZG)), along with the Drucker and Riser (2016) UW Argo Oxygen  
756 dataset which is now included in the Argo dataset (<https://argo.ucsd.edu/data/data-from-gdacs/>).  
757 Gridded Argo product by Roemmich and Gilson (2009) is available from  
758 <https://argo.ucsd.edu/data/argo-data-products/>. Argo data were collected and made freely  
759 available by the International Argo Program and the national programs that contribute to it  
760 (<http://doi.org/10.17882/42182>, <http://www.argo.ucsd.edu>, <http://argo.jcommops.org>).

761 Shipboard data are from SOCAT v2021 (Bakker et al., 2016;  
762 <https://www.socat.info/index.php/data-access/>) and GLODAP v2.2020 (Key et al., 2015; Olsen  
763 et al., 2016; <https://www.glodap.info/index.php/merged-and-adjusted-data-product/>).

764 Analysis and plotting code for this study are available at  
765 <https://doi.org/10.5281/zenodo.7349405> (Bushinsky and Cerovečki 2022).

766

767

768 **References**

- 769
- 770 Álvarez, M., C. Lo Monaco, T. Tanhua, and others. 2009. Estimating the storage of  
771 anthropogenic carbon in the subtropical Indian ocean: A comparison of five different  
772 approaches. *Biogeosciences* **6**: 681–703. doi:10.5194/bg-6-681-2009
- 773 Bakker, D. C. E., B. Pfeil, C. S. Landa, and others. 2016. A multi-decade record of high-quality  
774 fCO<sub>2</sub> data in version 3 of the Surface Ocean CO<sub>2</sub> Atlas (SOCAT). *Earth Syst. Sci. Data* **8**:  
775 383–413. doi:10.5194/essd-8-383-2016
- 776 de Boyer Montégut, C., G. Madec, A. S. Fischer, A. Lazar, and D. Iudicone. 2004. Mixed layer  
777 depth over the global ocean: An examination of profile data and a profile-based  
778 climatology. *J. Geophys. Res.* **109**: C12003. doi:10.1029/2004JC002378
- 779 Broecker, W. S., and T. H. Peng. 1982. Tracers in the Sea., Lamont-Doherty Earth Observatory.
- 780 Bushinsky, S., and I. Cerovečki. 2022. Subantarctic Mode Water Biogeochemical Formation  
781 Properties and Interannual Variability, analysis and plotting code  
782 (v1.1.1).doi:10.5281/zenodo.7349405
- 783 Bushinsky, S. M., A. R. Gray, K. S. Johnson, and J. L. Sarmiento. 2017. Oxygen in the Southern  
784 Ocean From Argo Floats: Determination of Processes Driving Air-Sea Fluxes. *J. Geophys.*  
785 *Res. Ocean.* **122**: 8661–8682. doi:10.1002/2017JC012923
- 786 Bushinsky, S. M., P. Landschützer, C. Rödenbeck, and others. 2019. Reassessing Southern  
787 Ocean Air-Sea CO<sub>2</sub> Flux Estimates With the Addition of Biogeochemical Float  
788 Observations. *Global Biogeochem. Cycles* **33**: 1370–1388. doi:10.1029/2019GB006176
- 789 Carter, B. R., R. A. Feely, S. K. Lauvset, and others. 2021. Preformed Properties for Marine  
790 Organic Matter and Carbonate Mineral Cycling Quantification. *Global Biogeochem. Cycles*  
791 **35**: 64–75. doi:10.1029/2020GB006623
- 792 Carter, B. R., R. A. Feely, N. L. Williams, and others. 2018. Updated methods for global locally  
793 interpolated estimation of alkalinity, pH, and nitrate. *Limnol. Oceanogr. Methods* **16**: 119–  
794 131. doi:10.1002/lom3.10232
- 795 Carter, B. R., L. D. Talley, and A. G. Dickson. 2014. Mixing and remineralization in waters  
796 detrained from the surface into Subantarctic Mode Water and Antarctic Intermediate Water  
797 in the southeastern Pacific. *J. Geophys. Res. Ocean.* **119**: 4001–4028.  
798 doi:10.1002/2013JC009355
- 799 Cerovečki, I., and M. R. Mazloff. 2016. The spatiotemporal structure of diabatic processes  
800 governing the evolution of Subantarctic Mode Water in the southern ocean. *J. Phys.*  
801 *Oceanogr.* **46**: 683–710. doi:10.1175/JPO-D-14-0243.1
- 802 Cerovečki, I., and A. J. S. Meijers. 2021. Strong quasi-stationary wintertime atmospheric surface  
803 pressure anomalies drive a dipole pattern in the Subantarctic Mode Water formation. *J.*  
804 *Clim.* 1–44. doi:10.1175/JCLI-D-20-0593.1
- 805 Cerovečki, I., A. J. S. Meijers, M. R. Mazloff, and others. 2019. The Effects of Enhanced Sea Ice  
806 Export from the Ross Sea on Recent Cooling and Freshening of the Southeast Pacific. *J.*  
807 *Clim.* **32**: 2013–2035. doi:10.1175/JCLI-D-18-0205.1
- 808 Dee, D. P., S. M. Uppala, A. J. Simmons, and others. 2011. The ERA-Interim reanalysis:  
809 Configuration and performance of the data assimilation system. *Q. J. R. Meteorol. Soc.* **137**:  
810 553–597. doi:10.1002/qj.828
- 811 DeVries, T. 2014. The oceanic anthropogenic CO<sub>2</sub> sink: Storage, air-sea fluxes, and transports  
812 over the industrial era. *Global Biogeochem. Cycles* **28**: 631–647.  
813 doi:10.1002/2013GB004739

- 814 Dlugokencky, E. J., K. W. Thoning, P. M. Lang, and P. P. Tans. 2019. NOAA Greenhouse Gas  
 815 Reference from Atmospheric Carbon Dioxide Dry Air Mole Fractions from the NOAA  
 816 ESRL Carbon Cycle Cooperative Global Air Sampling Network.
- 817 Downes, S. M., C. Langlais, J. P. Brook, and P. Spence. 2017. Regional impacts of the westerly  
 818 winds on Southern Ocean mode and intermediate water subduction. *J. Phys. Oceanogr.* **47**:  
 819 2521–2530. doi:10.1175/JPO-D-17-0106.1
- 820 Drucker, R., and S. C. Riser. 2016. In situ phase-domain calibration of oxygen Optodes on  
 821 profiling floats. *Methods Oceanogr.* **17**: 1–34. doi:10.1016/j.mio.2016.09.007
- 822 Duteil, O., W. Koeve, A. Oschlies, and others. 2013. A novel estimate of ocean oxygen  
 823 utilisation points to a reduced rate of respiration in the ocean interior. *Biogeosciences* **10**:  
 824 7723–7738. doi:10.5194/bg-10-7723-2013
- 825 Fay, A. R., N. S. Lovenduski, G. A. McKinley, and others. 2018. Utilizing the Drake Passage  
 826 Time-series to understand variability and change in subpolar Southern Ocean pCO<sub>2</sub>.  
 827 *Biogeosciences Discuss.* doi:https://doi.org/10.5194/bg-2017-489
- 828 Fay, A. R., G. A. McKinley, and N. S. Lovenduski. 2014. Southern Ocean carbon trends:  
 829 Sensitivity to methods. *Geophys. Res. Lett.* **41**: 6833–6840. doi:10.1002/2014GL061324
- 830 Fernández Castro, B., M. Mazloff, R. G. Williams, and A. C. Naveira Garabato. 2022.  
 831 Subtropical contribution to Sub-Antarctic Mode Waters. *Geophys. Res. Lett.*  
 832 doi:10.1029/2021gl097560
- 833 Gao, L., S. R. Rintoul, and W. Yu. 2018. Recent wind-driven change in Subantarctic Mode  
 834 Water and its impact on ocean heat storage. *Nat. Clim. Chang.* **8**: 58–63.  
 835 doi:10.1038/s41558-017-0022-8
- 836 García, H. E., and L. I. Gordon. 1992. Oxygen solubility in seawater: Better fitting equations.  
 837 *Limnol. Oceanogr.* **37**: 1307–1312. doi:10.4319/lo.1992.37.6.1307
- 838 Garcia, H. E., R. A. Locarnini, T. P. Boyer, and others. 2010. World Ocean Atlas 2009 Volume  
 839 3: Dissolved Oxygen, Apparent Oxygen Utilization, and Oxygen Saturation.
- 840 Gray, A. R., K. S. Johnson, S. M. Bushinsky, and others. 2018. Autonomous Biogeochemical  
 841 Floats Detect Significant Carbon Dioxide Outgassing in the High-Latitude Southern Ocean.  
 842 *Geophys. Res. Lett.* **45**: 9049–9057. doi:10.1029/2018GL078013
- 843 Groeskamp, S., A. Lenton, R. Matear, B. M. Sloyan, and C. Langlais. 2016. Anthropogenic  
 844 carbon in the ocean—Surface to interior connections. *Global Biogeochem. Cycles* **30**:  
 845 1682–1698. doi:10.1002/2016GB005476
- 846 Gruber, N., D. Clement, B. R. Carter, and others. 2019a. The oceanic sink for anthropogenic CO  
 847 2 from 1994 to 2007. *Science (80-. )*. **363**: 1193–1199. doi:10.1126/science.aau5153
- 848 Gruber, N., S. C. Doney, S. R. Emerson, and others. 2009a. Adding oxygen to Argo: Developing  
 849 a global in-situ observatory for ocean deoxygenation and biogeochemistry. *Ocean Obs '09*.
- 850 Gruber, N., M. Gloor, S. E. Mikaloff Fletcher, and others. 2009b. Oceanic sources, sinks, and  
 851 transport of atmospheric CO<sub>2</sub>. *Global Biogeochem. Cycles* **23**: n/a-n/a.  
 852 doi:10.1029/2008GB003349
- 853 Gruber, N., P. Landschützer, and N. S. Lovenduski. 2019b. The Variable Southern Ocean  
 854 Carbon Sink. *Ann. Rev. Mar. Sci.* **11**: 159–186. doi:10.1146/annurev-marine-121916-  
 855 063407
- 856 Hanawa, K., and L. Talley. 2001. Mode waters, p. 373–386. *In International Geophysics*.
- 857 Hartin, C. A., R. A. Fine, B. M. Sloyan, and others. 2011. Formation rates of Subantarctic mode  
 858 water and Antarctic intermediate water within the South Pacific. *Deep. Res. Part I*  
 859 *Oceanogr. Res. Pap.* **58**: 524–534. doi:10.1016/j.dsr.2011.02.010

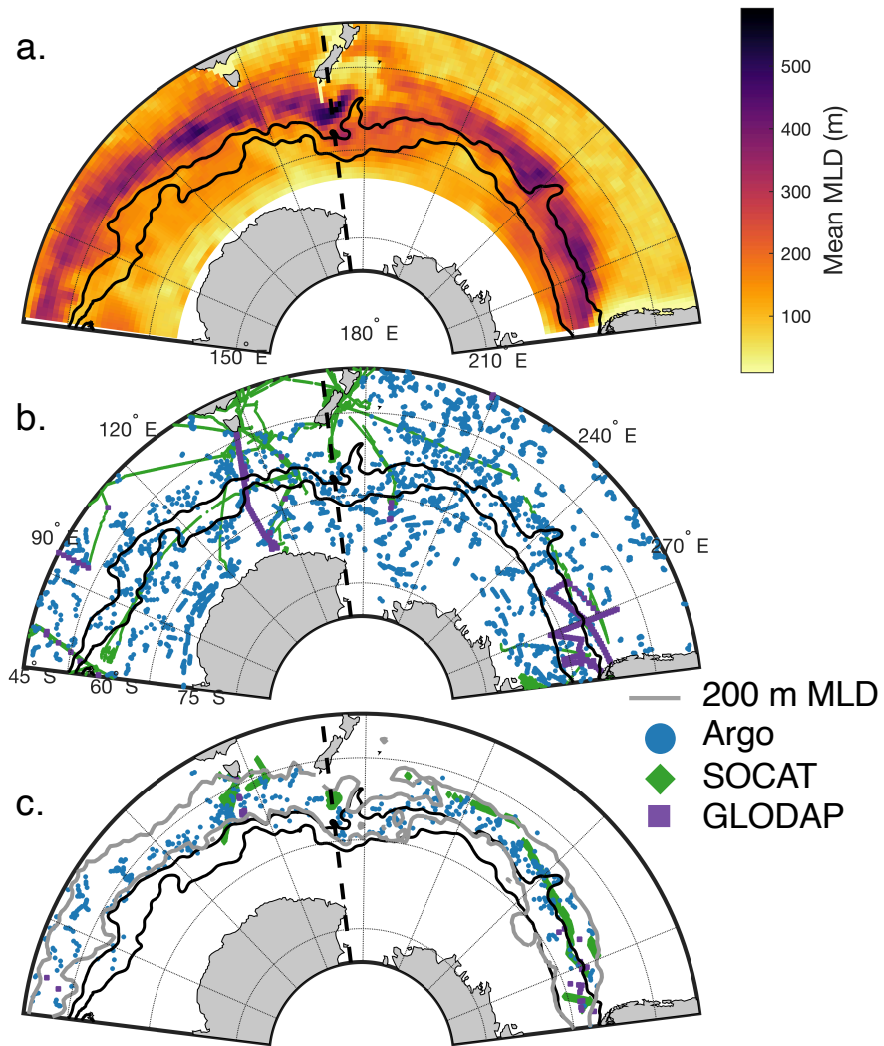
- 860 Herraiz-Borreguero, L., and S. R. Rintoul. 2011. Subantarctic mode water: Distribution and  
861 circulation. *Ocean Dyn.* **61**: 103–126. doi:10.1007/s10236-010-0352-9
- 862 van Heuven, S. M. A. C., D. Pierrot, J. W. B. Rae, E. Lewis, and D. W. R. Wallace. 2011.  
863 Matlab program developed for CO<sub>2</sub> system calculations. 530.
- 864 Ito, T., M. J. Follows, and E. A. Boyle. 2004. Is AOU a good measure of respiration in the  
865 oceans? *Geophys. Res. Lett.* **31**: n/a-n/a. doi:10.1029/2004GL020900
- 866 Iudicone, D., K. B. Rodgers, Y. Plancherel, and others. 2016. The formation of the ocean's  
867 anthropogenic carbon reservoir. *Sci. Rep.* **6**: 35473. doi:10.1038/srep35473
- 868 Iudicone, D., K. B. Rodgers, I. Stendardo, and others. 2011. Water masses as a unifying  
869 framework for understanding the Southern Ocean Carbon Cycle. *Biogeosciences* **8**: 1031–  
870 1052. doi:10.5194/bg-8-1031-2011
- 871 Johnson, K. S., J. N. Plant, L. J. Coletti, and others. 2017. Biogeochemical sensor performance in  
872 the SOCCOM profiling float array. *J. Geophys. Res. Ocean.* **122**: 6416–6436.  
873 doi:10.1002/2017JC012838
- 874 Kalnay, E., M. Kanamitsu, R. Kistler, and others. 1996. The NCEP/NCAR 40-Year Reanalysis  
875 Project. *Bull. Am. Meteorol. Soc.* **77**: 437–471. doi:http://dx.doi.org/10.1175/1520-  
876 0477(1996)077<0437:TNYRP>2.0.CO;2
- 877 Key, R. M., A. Olsen, S. van Heuven, and others. 2015. Global Ocean Data Analysis Project,  
878 Version 2 (GLODAPv2). ORNL/CDIAC-162, NDP-093.  
879 doi:10.3334/CDIAC/OTG.NDP093\_GLODAPv2
- 880 Koch-Larrouy, A., R. Morrow, T. Penduff, and M. Juza. 2010. Origin and mechanism of  
881 Subantarctic Mode Water formation and transformation in the Southern Indian Ocean.  
882 *Ocean Dyn.* **60**: 563–583. doi:10.1007/s10236-010-0276-4
- 883 Koeve, W., and P. Kähler. 2016. Oxygen utilization rate (OUR) underestimates ocean  
884 respiration: A model study. *Global Biogeochem. Cycles* **30**: 1166–1182.  
885 doi:10.1002/2015GB005354
- 886 Kolodziejczyk, N., W. Llovel, and E. Portela. 2019. Interannual Variability of Upper Ocean  
887 Water Masses as Inferred From Argo Array. *J. Geophys. Res. Ocean.* **124**: 6067–6085.  
888 doi:10.1029/2018JC014866
- 889 Landschützer, P., N. Gruber, D. C. E. Bakker, and others. 2013. A neural network-based estimate  
890 of the seasonal to inter-annual variability of the Atlantic Ocean carbon sink. *Biogeosciences*  
891 **10**: 7793–7815. doi:10.5194/bg-10-7793-2013
- 892 Landschützer, P., N. Gruber, and D. C. E. Bakker. 2016. Decadal variations and trends of the  
893 global ocean carbon sink. *Global Biogeochem. Cycles* **30**. doi:10.1002/2015GB005359
- 894 Landschützer, P., N. Gruber, F. A. Haumann, and others. 2015. The reinvigoration of the  
895 Southern Ocean carbon sink. *Science (80-. )*. **349**: 1221–1224. doi:10.1126/science.aab2620
- 896 Lauvset, S., K. Currie, N. Metzl, and others. 2017. SOCAT Quality Control Cookbook: for  
897 SOCAT version 7. SOCAT. doi:http://dx.doi.org/10.25607/OBP-1665
- 898 Lauvset, S. K., R. M. Key, A. Olsen, and others. 2016. A new global interior ocean mapped  
899 climatology: The 1° × 1° GLODAP version 2. *Earth Syst. Sci. Data* **8**: 325–340.  
900 doi:10.5194/essd-8-325-2016
- 901 Lenton, A., and R. J. Matear. 2007. Role of the Southern Annular Mode (SAM) in Southern  
902 Ocean CO<sub>2</sub> uptake. *Global Biogeochem. Cycles* **21**: 1–17. doi:10.1029/2006GB002714
- 903 Li, Z., M. H. England, S. Groeskamp, I. Cerovečki, and Y. Luo. 2021. The Origin and Fate of  
904 Subantarctic Mode Water in the Southern Ocean. *J. Phys. Oceanogr.* 2951–2972.  
905 doi:10.1175/jpo-d-20-0174.1

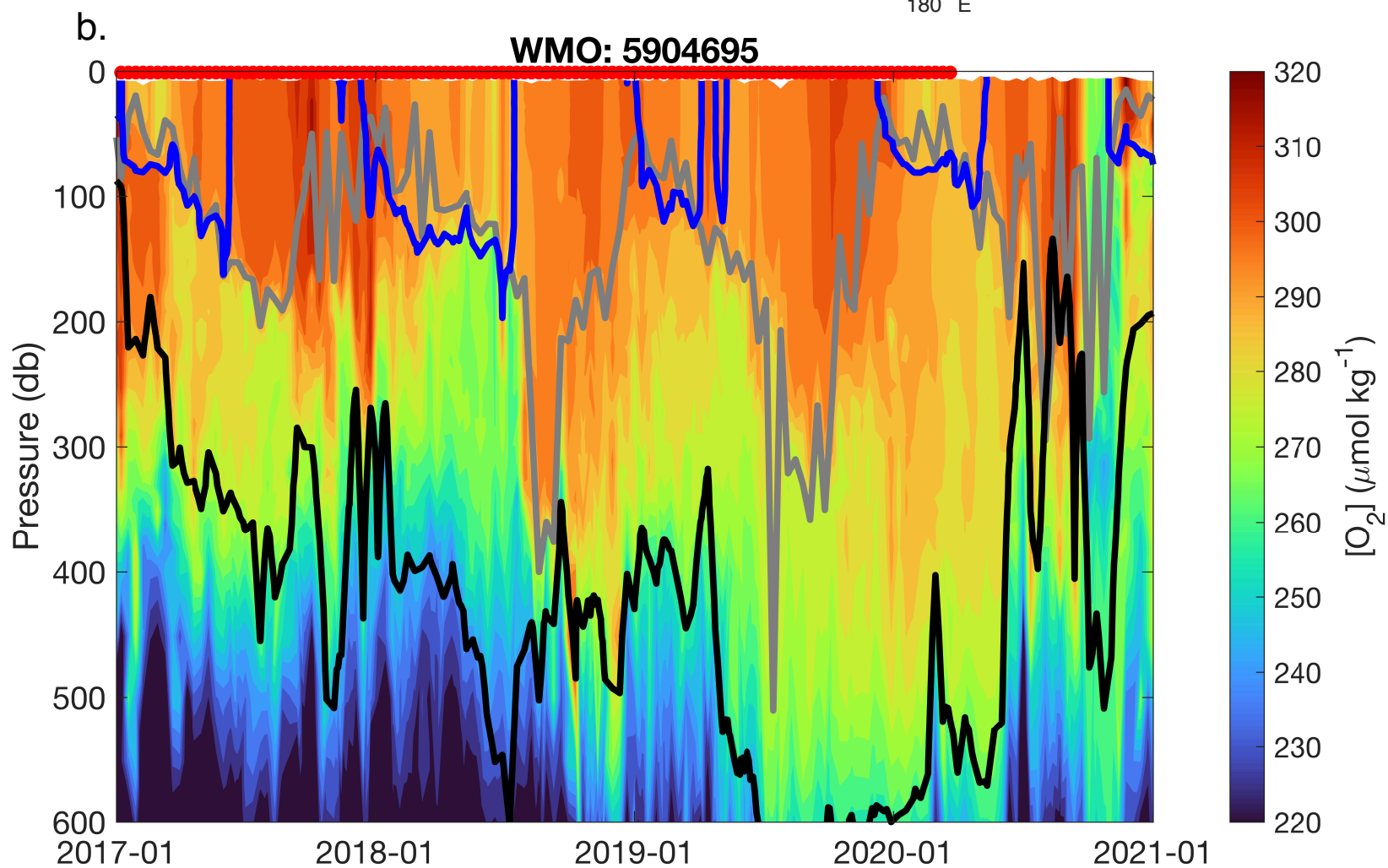
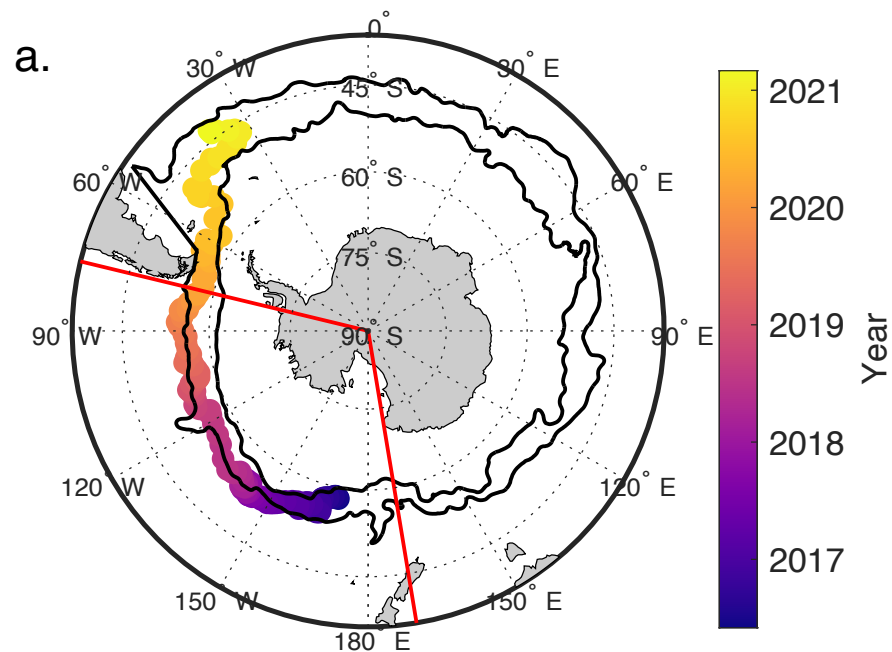


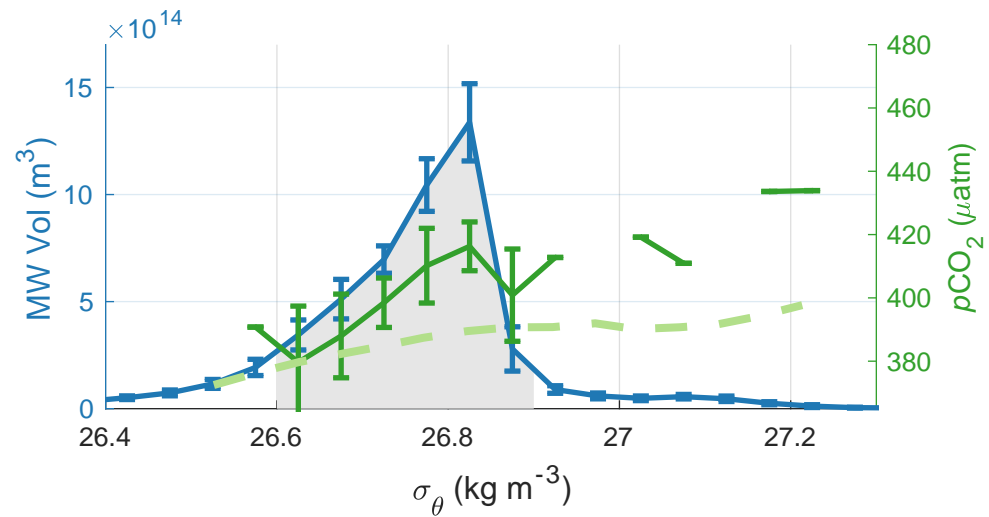
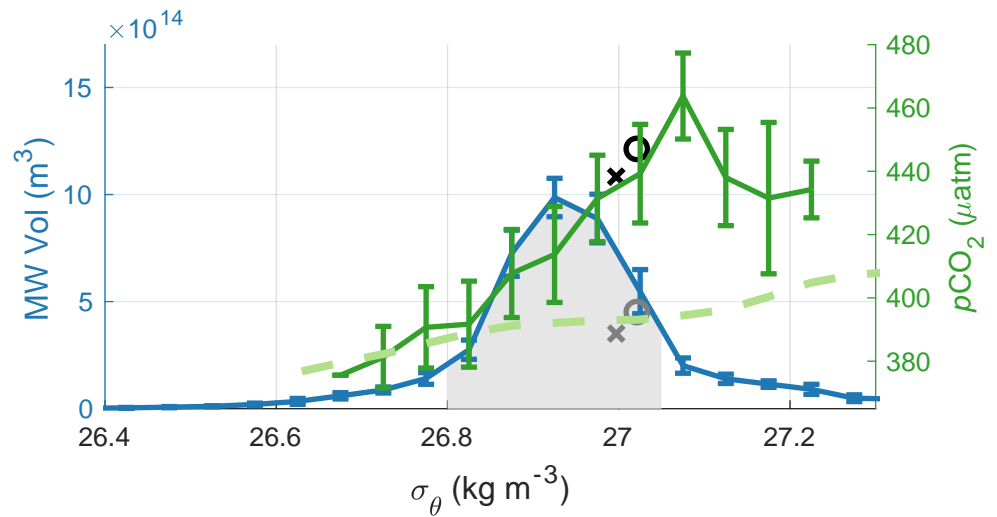
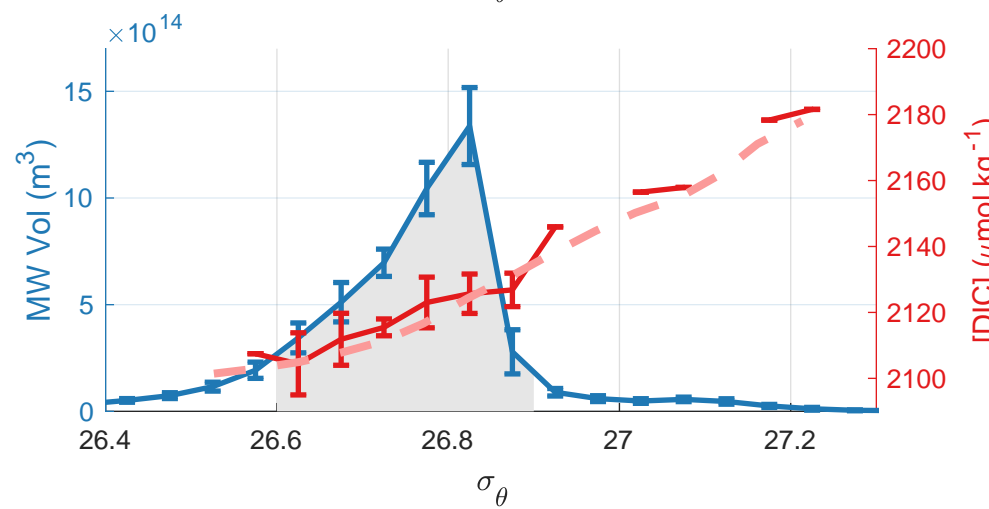
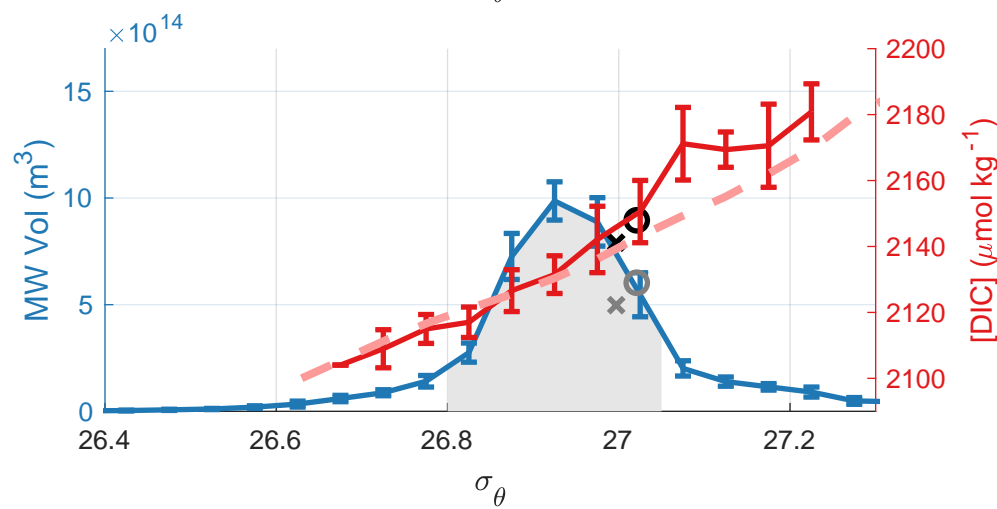
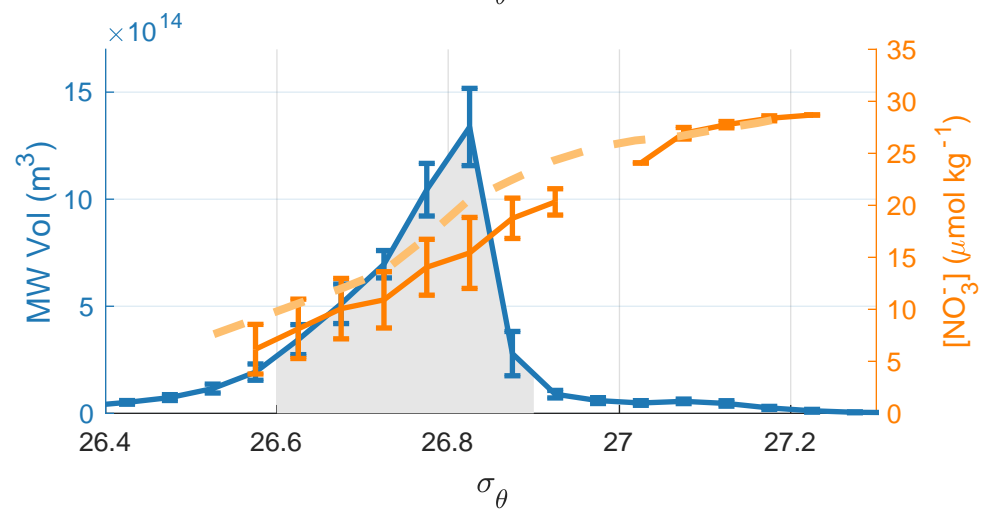
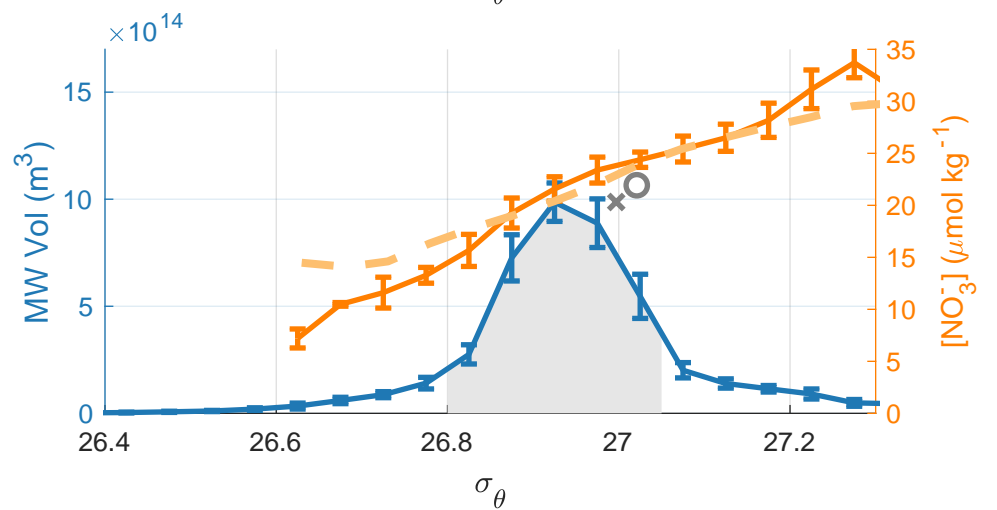
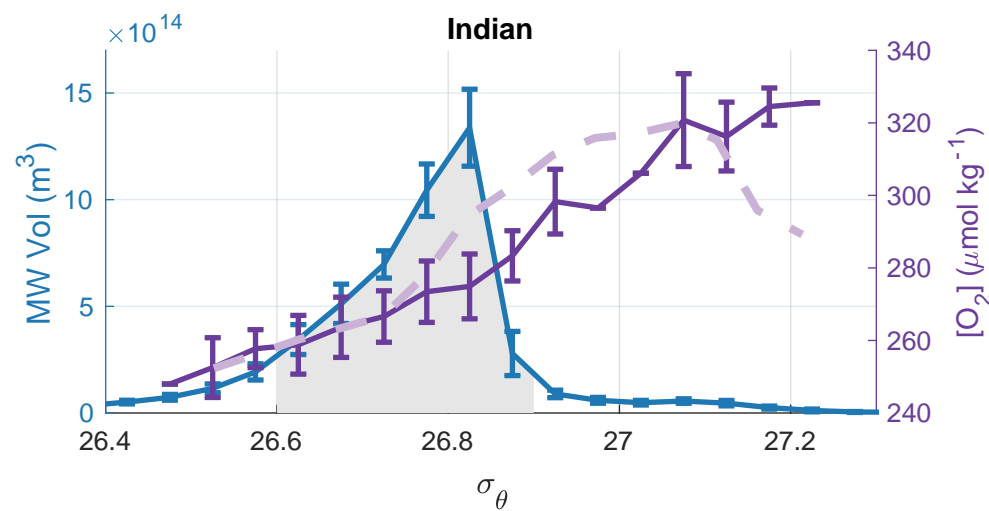
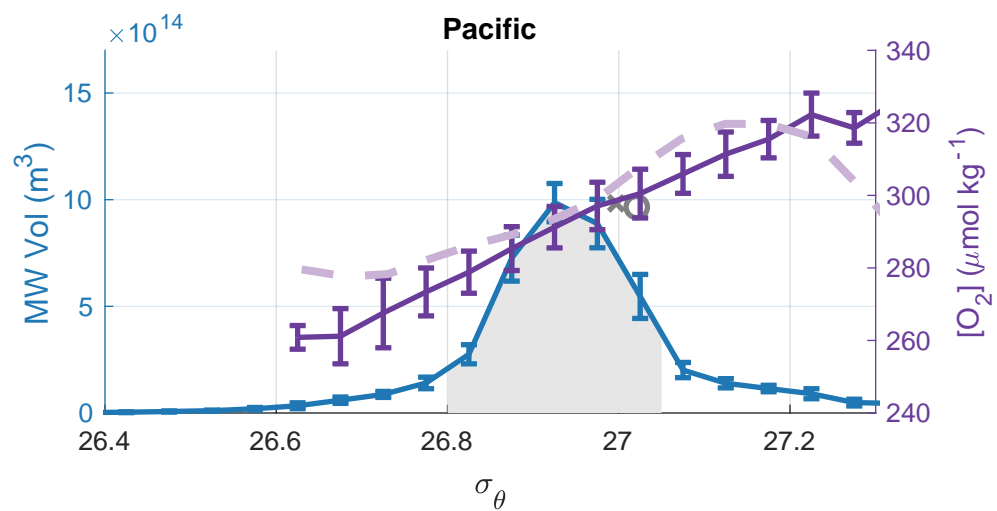
- 906 Long, M. C., B. B. Stephens, K. McKain, and others. 2021. Strong Southern Ocean carbon  
 907 uptake evident in airborne observations. *Science* (80-. ). **374**: 1275–1280.  
 908 doi:10.1126/science.abi4355
- 909 Lovenduski, N. S., N. Gruber, S. C. Doney, and I. D. Lima. 2007. Enhanced CO<sub>2</sub> outgassing in  
 910 the Southern Ocean from a positive phase of the Southern Annular Mode. *Global*  
 911 *Biogeochem. Cycles* **21**: n/a-n/a. doi:10.1029/2006GB002900
- 912 Mackay, N., and A. Watson. 2021. Winter air-sea CO<sub>2</sub> fluxes constructed from summer  
 913 observations of the Polar Southern Ocean suggest weak outgassing . *J. Geophys. Res.*  
 914 *Ocean*. doi:10.1029/2020jc016600
- 915 Maurer, T. L., J. N. Plant, and K. S. Johnson. 2021. Delayed-Mode Quality Control of Oxygen,  
 916 Nitrate, and pH Data on SOCCOM Biogeochemical Profiling Floats. *Front. Mar. Sci.* **8**: 1–  
 917 20. doi:10.3389/fmars.2021.683207
- 918 McCartney, M. 1982. The subtropical recirculation of mode waters. *J. Mar. Res* **40**: 427–464.
- 919 McCartney, M. S. 1977. Subantarctic Mode Water, p. 103–119. *In* M. Angel [ed.], *A Voyage of*  
 920 *Discovery: George Deacon 70th Anniversary Volume*.
- 921 Meijers, A. J. S., I. Cerovečki, B. A. King, and V. Tamsitt. 2019. A See-Saw in Pacific  
 922 Subantarctic Mode Water Formation Driven by Atmospheric Modes. *Geophys. Res. Lett.*  
 923 **46**: 13152–13160. doi:10.1029/2019GL085280
- 924 Mikaloff Fletcher, S. E., N. Gruber, A. R. Jacobson, and others. 2006. Inverse estimates of  
 925 anthropogenic CO<sub>2</sub> uptake, transport, and storage by the ocean. *Global Biogeochem.*  
 926 *Cycles* **20**: n/a-n/a. doi:10.1029/2005GB002530
- 927 Mikaloff Fletcher, S. E., N. Gruber, A. R. Jacobson, and others. 2007. Inverse estimates of the  
 928 oceanic sources and sinks of natural CO<sub>2</sub> and the implied oceanic carbon transport. *Global*  
 929 *Biogeochem. Cycles* **21**: 1–19. doi:10.1029/2006GB002751
- 930 Mongwe, N. P., M. Vichi, and P. M. S. Monteiro. 2018. The seasonal cycle of p CO<sub>2</sub> and CO<sub>2</sub>  
 931 fluxes in the Southern Ocean: diagnosing anomalies in CMIP5 Earth system models.  
 932 *Biogeosciences* **15**: 2851–2872. doi:10.5194/bg-15-2851-2018
- 933 Morrison, A. K., T. L. Frölicher, and J. L. Sarmiento. 2015. Upwelling in the Southern Ocean.  
 934 *Phys. Today* **68**: 27–32. doi:10.1063/PT.3.2654
- 935 Morrison, A. K., D. W. Waugh, A. M. Hogg, D. C. Jones, and R. P. Abernathy. 2022.  
 936 Ventilation of the Southern Ocean Pycnocline. *Ann. Rev. Mar. Sci.* **14**: 405–430.  
 937 doi:10.1146/annurev-marine-010419-011012
- 938 Olsen, A., R. M. Key, S. Van Heuven, and others. 2016. The global ocean data analysis project  
 939 version 2 (GLODAPv2) - An internally consistent data product for the world ocean. *Earth*  
 940 *Syst. Sci. Data* **8**: 297–323. doi:10.5194/essd-8-297-2016
- 941 Portela, E., N. Kolodziejczyk, C. Maes, and V. Thierry. 2020. Interior Water-Mass Variability in  
 942 the Southern Hemisphere Oceans during the Last Decade. *J. Phys. Oceanogr.* **50**: 361–381.  
 943 doi:10.1175/JPO-D-19-0128.1
- 944 Primeau, F. W., M. Holzer, and T. DeVries. 2013. Southern Ocean nutrient trapping and the  
 945 efficiency of the biological pump. *J. Geophys. Res. Ocean.* **118**: 2547–2564.  
 946 doi:10.1002/jgrc.20181
- 947 Qu, T., S. Gao, and R. A. Fine. 2020. Variability of the Sub-Antarctic Mode Water Subduction  
 948 Rate During the Argo Period. *Geophys. Res. Lett.* **47**. doi:10.1029/2020GL088248
- 949 Raphael, M. N. 2004. A zonal wave 3 index for the Southern Hemisphere. *Geophys. Res. Lett.*  
 950 **31**: 1–4. doi:10.1029/2004GL020365
- 951 Rintoul, S. R., and M. H. England. 2002. Ekman transport dominates local air-sea fluxes in

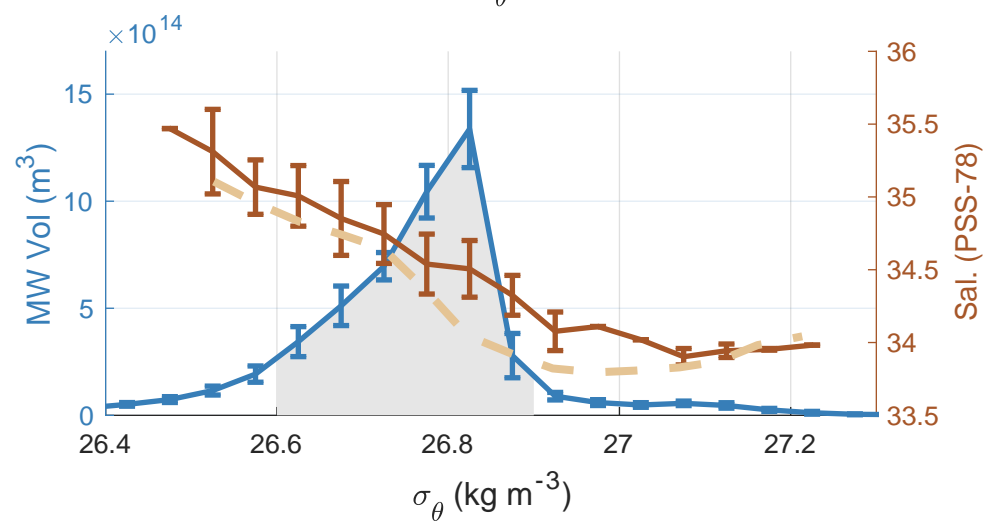
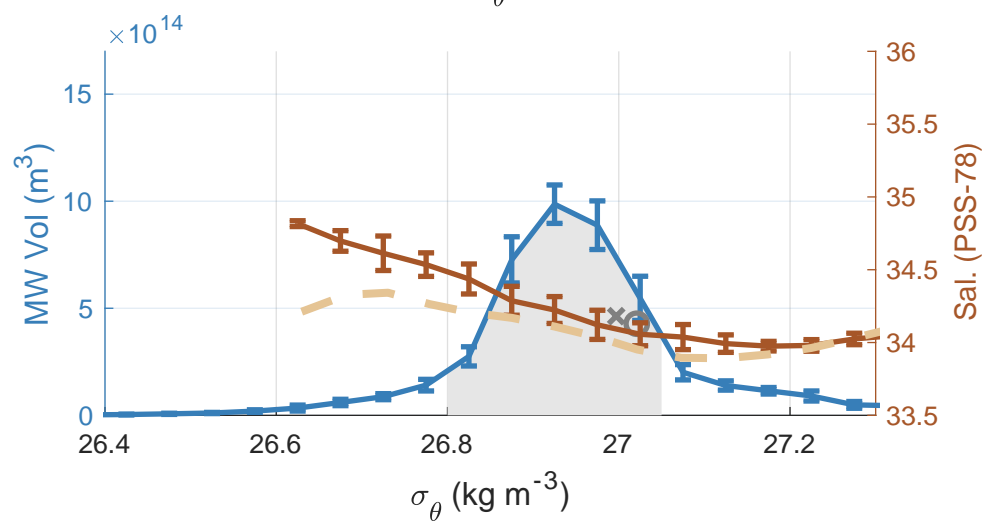
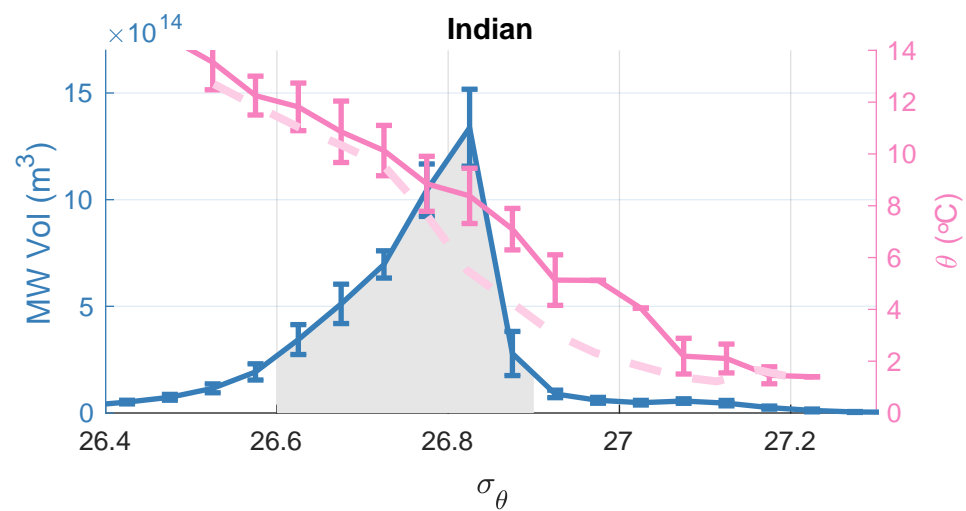
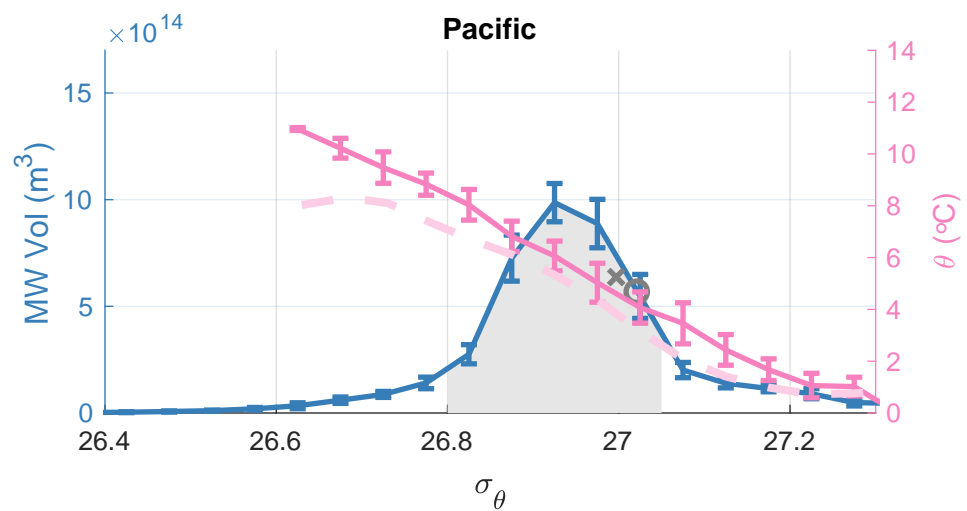
- 952 driving variability of subantarctic mode water. *J. Phys. Oceanogr.* **32**: 1308–1321.  
953 doi:10.1175/1520-0485(2002)032<1308:ETDLAS>2.0.CO;2
- 954 Rödenbeck, C., R. F. Keeling, D. C. E. Bakker, and others. 2013. Global surface-ocean pCO<sub>2</sub>  
955 and sea-Air CO<sub>2</sub> flux variability from an observation-driven ocean mixed-layer scheme.  
956 *Ocean Sci.* **9**: 193–216. doi:10.5194/os-9-193-2013
- 957 Roemmich, D., and J. Gilson. 2009. The 2004–2008 mean and annual cycle of temperature,  
958 salinity, and steric height in the global ocean from the Argo Program. *Prog. Oceanogr.* **82**:  
959 81–100. doi:10.1016/j.pocean.2009.03.004
- 960 Russell, J. L., and A. G. Dickson. 2003. Variability in oxygen and nutrients in South Pacific  
961 Antarctic Intermediate Water. *Global Biogeochem. Cycles* **17**: n/a-n/a.  
962 doi:10.1029/2000GB001317
- 963 Sabine, C. L., R. A. Feely, N. Gruber, and others. 2004. The Oceanic Sink for Anthropogenic  
964 CO<sub>2</sub>. *Science* (80-. ). **305**: 367–371.
- 965 Sabine, C. L., and T. Tanhua. 2010. Estimation of Anthropogenic CO<sub>2</sub> Inventories in the Ocean.  
966 *Ann. Rev. Mar. Sci.* **2**: 175–198. doi:10.1146/annurev-marine-120308-080947
- 967 Sallée, J. B., K. G. Speer, and S. R. Rintoul. 2010. Zonally asymmetric response of the Southern  
968 Ocean mixed-layer depth to the Southern Annular Mode. *Nat. Geosci.* **3**: 273–279.  
969 doi:10.1038/ngeo812
- 970 Sarmiento, J. L., N. Gruber, M. A. Brzezinski, and J. P. Dunne. 2004. High-latitude controls of  
971 thermocline nutrients and low latitude biological productivity. *Nature* **427**: 56–60.  
972 doi:10.1038/nature10605
- 973 Sloyan, B. M., and S. R. Rintoul. 2001. The Southern Ocean Limb of the Global Deep  
974 Overturning Circulation\*. *J. Phys. Oceanogr.* **31**: 143–173. doi:10.1175/1520-  
975 0485(2001)031<0143:TSOLOT>2.0.CO;2
- 976 Speer, K., S. R. Rintoul, and B. Sloyan. 2000. The Diabatic Deacon Cell\*. *J. Phys. Oceanogr.*  
977 **30**: 3212–3222. doi:10.1175/1520-0485(2000)030<3212:TDDC>2.0.CO;2
- 978 Sutton, A. J., N. L. Williams, and B. Tilbrook. 2021. Constraining Southern Ocean CO<sub>2</sub> Flux  
979 Uncertainty Using Uncrewed Surface Vehicle Observations. *Geophys. Res. Lett.* **48**: 1–9.  
980 doi:10.1029/2020GL091748
- 981 Tamsitt, V., I. Cerovečki, S. A. Josey, S. T. Gille, and E. Schulz. 2020. Mooring Observations of  
982 Air–Sea Heat Fluxes in Two Subantarctic Mode Water Formation Regions. *J. Clim.* **33**:  
983 2757–2777. doi:10.1175/JCLI-D-19-0653.1
- 984 Verdy, A., S. Dutkiewicz, M. J. Follows, J. Marshall, and A. Czaja. 2007. Carbon dioxide and  
985 oxygen fluxes in the Southern Ocean: Mechanisms of interannual variability. *Global*  
986 *Biogeochem. Cycles* **21**: 1–10. doi:10.1029/2006GB002916
- 987 Verdy, A., and M. R. Mazloff. 2017. A data assimilating model for estimating Southern Ocean  
988 biogeochemistry. *J. Geophysical Res. Ocean.* **122**: 1–22. doi:10.1002/2016JC012650
- 989 Williams, N. L., L. W. Juranek, R. A. Feely, and others. 2017. Calculating surface ocean pCO<sub>2</sub>  
990 from biogeochemical Argo floats equipped with pH: An uncertainty analysis. *Global*  
991 *Biogeochem. Cycles* **31**: 591–604. doi:10.1002/2016GB005541
- 992 Williams, N. L., L. W. Juranek, R. A. Feely, and others. 2018. Assessment of the carbonate  
993 chemistry seasonal cycles in the Southern Ocean from persistent observational platforms. *J.*  
994 *Geophys. Res. Ocean.* **123**: 1–20. doi:10.1029/2017JC012917
- 995 Wolf, M. K., R. C. Hamme, D. Gilbert, I. Yashayaev, and V. Thierry. 2018. Oxygen Saturation  
996 Surrounding Deep Water Formation Events in the Labrador Sea From Argo-O<sub>2</sub> Data.  
997 *Global Biogeochem. Cycles* **32**: 635–653. doi:10.1002/2017GB005829

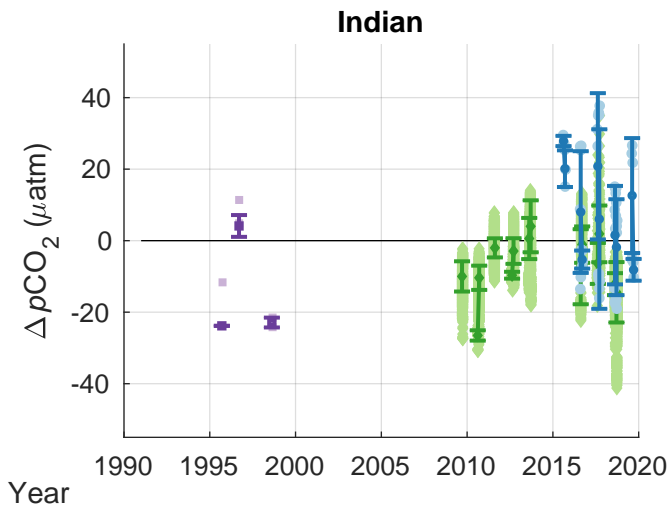
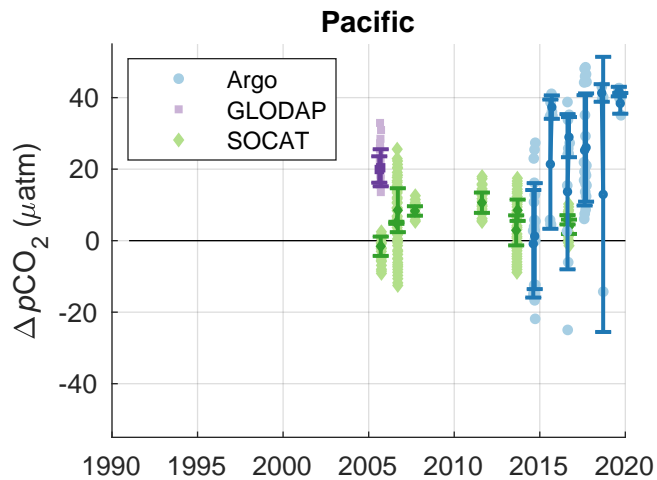
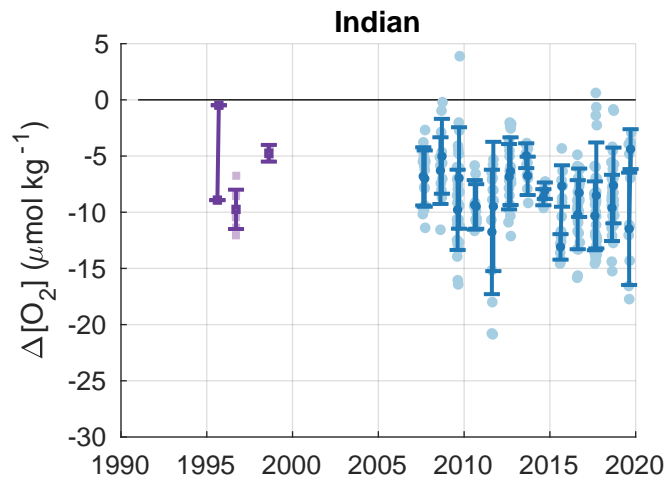
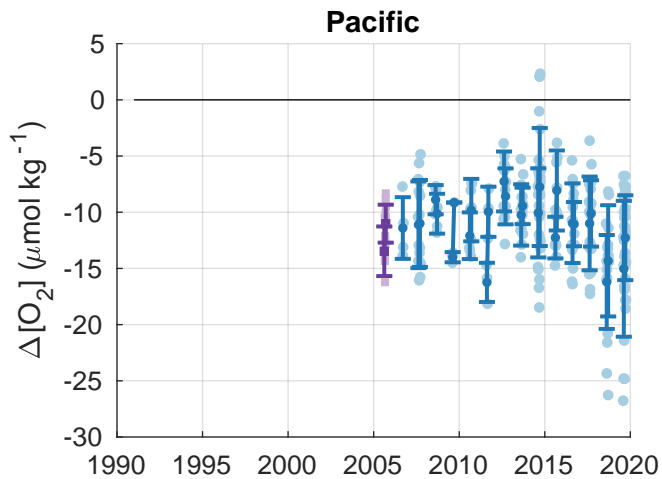
998 Wong, A. P. S., N. L. Bindoff, and J. A. Church. 1999. Large-scale freshening of intermediate  
999 waters in the Pacific and Indian oceans. *Nature* **400**: 440–443. doi:10.1038/22733  
1000 Wu, Y., D. C. E. Bakker, E. P. Achterberg, and others. 2022. Integrated analysis of carbon  
1001 dioxide and oxygen concentrations as a quality control of ocean float data. *Commun. Earth*  
1002 *Environ.* **3**: 92. doi:10.1038/s43247-022-00421-w  
1003 Zeebe, R. E., and D. A. Wolf-Gladrow. 2001. *CO<sub>2</sub> in Seawater: Equilibrium, Kinetics, Isotopes*,  
1004 Elsevier.  
1005



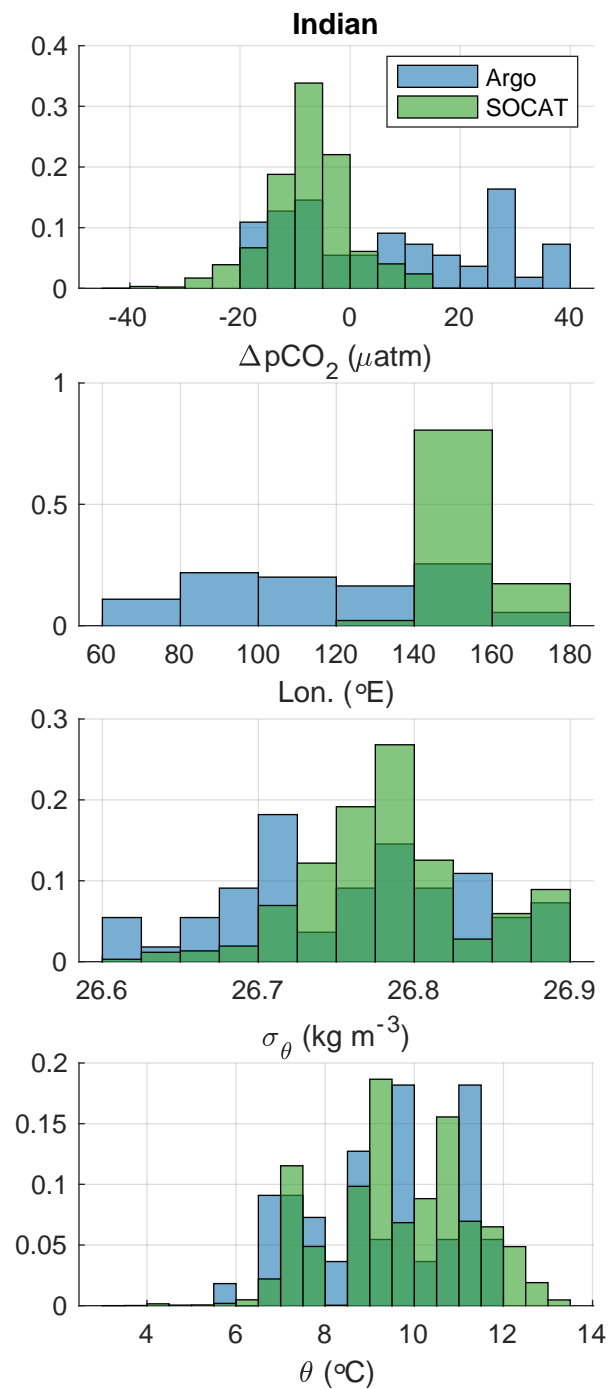
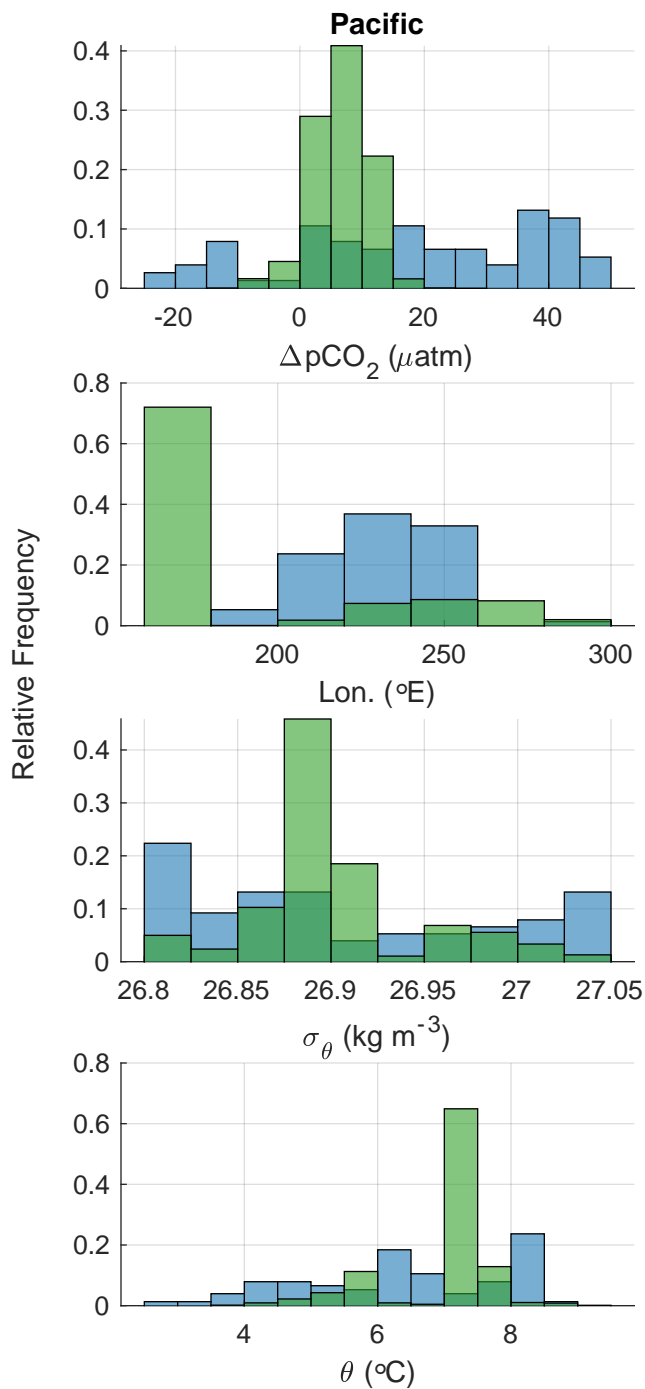


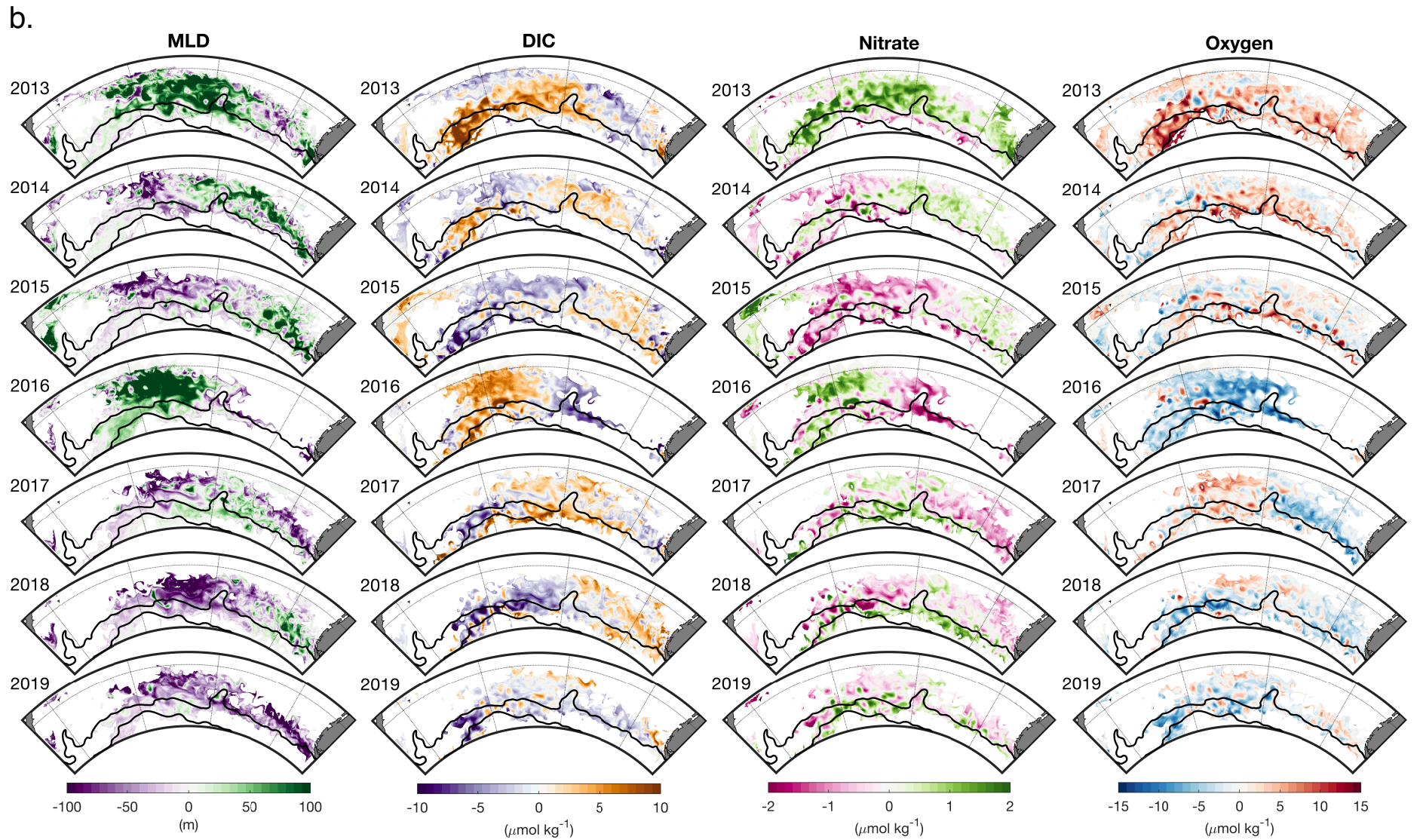
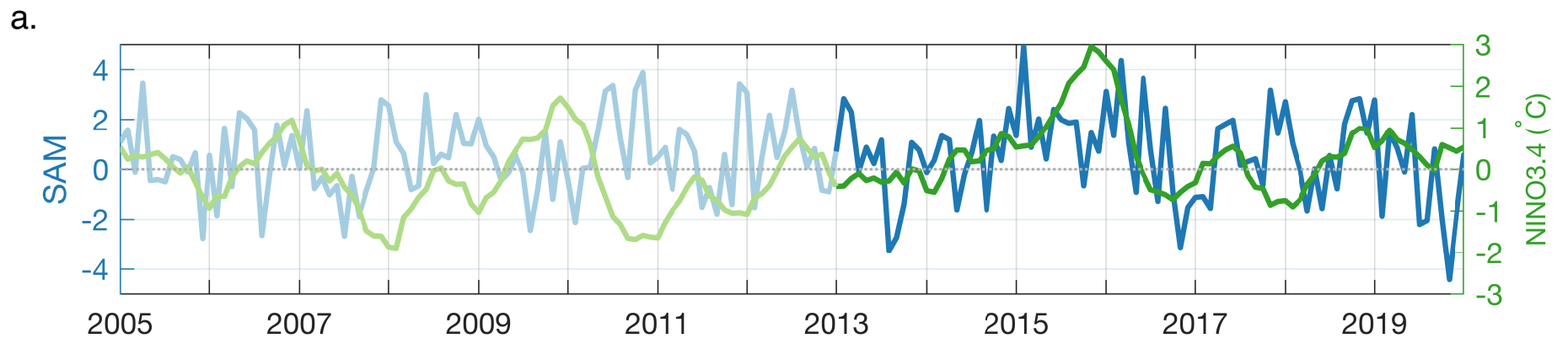


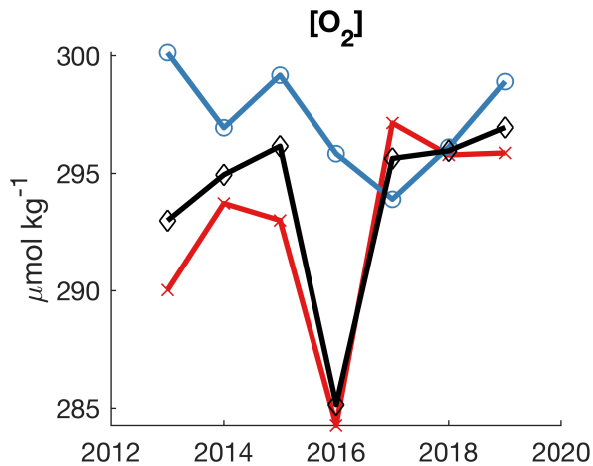
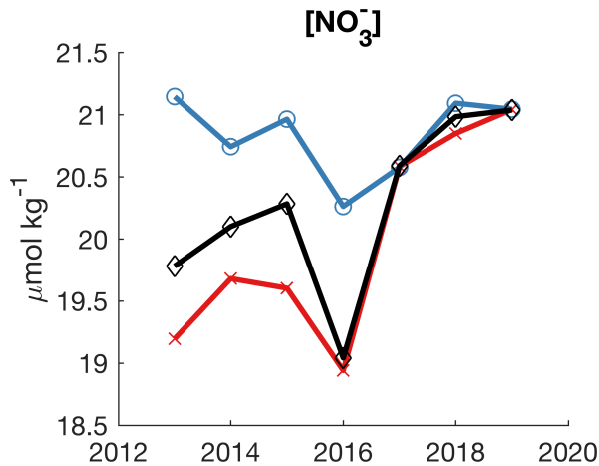
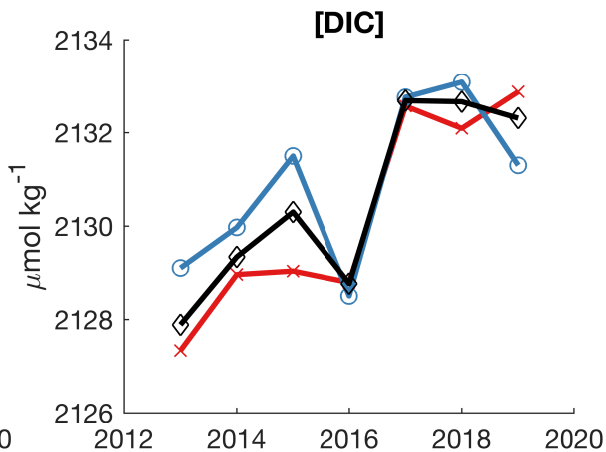
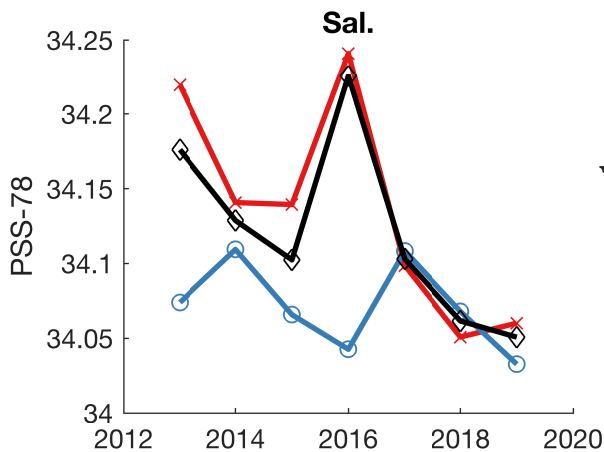
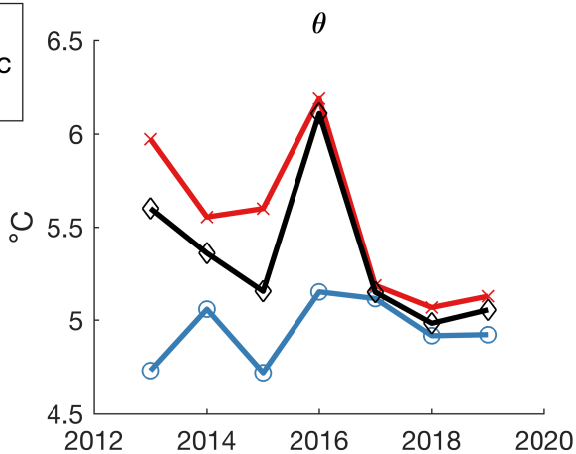
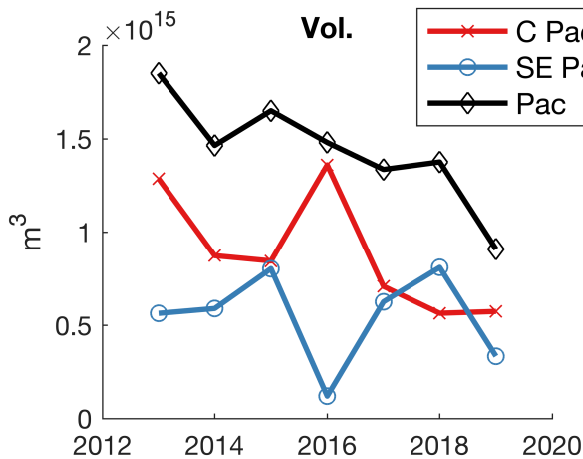












Year